Removing numerical pathologies in a turbulence parameterization through convergence testing

Shixuan Zhang[1], Christopher J. Vogl[2], Vincent E. Larson[1,3], Quan M. Bui[2,4], Hui Wan[1], Philip J. Rasch[1], Carol S. Woodward[2]

[1]Atmospheric Sciences and Global Change Division, Pacific Northwest National Laboratory, Richland, Washington, USA
[2]Center for Applied Scientific Computing, Lawrence Livermore National Laboratory, Livermore, California, USA
[3]Department of Mathematical Sciences, University of Wisconsin–Milwaukee, Milwaukee, Wisconsin, USA
[4]Blue River Technology, Sunnyvale, California, USA

Key Points:

- Use of numerical limiters can inject sawtooth noise into model solutions. Background diffusion can amplify the noise and damage convergence.
- Improved treatment of limiters and background diffusion can reduce noise and improve the quality of solutions and numerical convergence.
- Convergence testing is a valuable tool for detecting noise in the model solution, as well as unintended discontinuities and grid dependence.

Corresponding author: Shixuan Zhang, Christopher Vogl, Vincent E. Larson,
Shixuan.Zhang@pnnl.gov, Vogl, vogl2@llnl.gov, vlarson@uwm.edu

Abstract

Discretized numerical models of the atmosphere are usually intended to faithfully represent an underlying set of continuous equations, but this necessary condition is violated sometimes by subtle pathologies that have crept into the discretized equations. Such pathologies can introduce undesirable artifacts, such as sawtooth noise, into the model solutions. The presence of these pathologies can be detected by numerical convergence testing. This study employs convergence testing to verify the discretization of the Cloud Layers Unified By Binormals (CLUBB) model of clouds and turbulence. That convergence testing identifies two aspects of CLUBB's equation set that contribute to undesirable noise in the solutions. First, numerical limiters (i.e. clipping) used by CLUBB introduce discontinuities or slope discontinuities in model fields. Second, this noise can be amplified by an advective term in CLUBB's background diffusion. Smoothing the limiters and removing the advective component of the background diffusion reduces the noise and restores the expected first-order convergence in CLUBB's solutions. These model reformulations improve the results at coarser, near-operational grid spacing and time step in cumulus cloud and dry turbulence tests. In addition, convergence testing is proved to be a valuable tool for detecting pathologies, including unintended discontinuities and grid dependence, in the model equation set.

Plain Language Summary

In order to detect pathologies in a numerical model of the atmosphere, a diagnostic test is used here that has been widely adopted in the applied mathematics community. The diagnostic test, if set up properly, proves to be effective at detecting the pathologies. Both the method of testing and the particular pathologies detected are expected to be relevant to other atmospheric models.

1 Introduction

An important aspect of numerical modeling of the atmosphere is developing physical understanding of model solutions. Understanding helps us to formulate new scientific hypotheses and to build confidence in the model. Our intuition about nature comes from continuous equations, the first principles behind those equations, and the observations that result from those equations. However, our ability to apply our intuition to a model's behavior may be confounded if the discretized model equations do not faithfully represent the continuous equations. The solutions from such improperly discretized model equations may contain numerical artifacts that lead to confusing model behavior, such as spurious intermittent spikes. Those solutions may also be more sensitive to grid or timestep refinement than solutions from properly discretized model equations. In such cases, the sensitivity of the improperly discretized model will require more labor-intensive retuning, compared to a properly discretized model, whenever the grid or timestep is refined (Wan et al., 2021).

A standard tool for identifying improperly discretized model equations is convergence testing (e.g. Roache, 1998; Knupp & Salari, 2002; Oberkampf et al., 2004). If the solutions from a discretized model do not converge to a reference solution at a theoretically determined rate, e.g. proportional to grid spacing and timestep, the test confirms the presence of one or more pathologies in the discretized equation set. Those pathologies will certainly damage the solutions at fine resolution, and can damage the solutions at operational resolution, including significantly affecting clouds in a global simulation (Wan et al., 2020; Vogl et al., 2020). Other pathologies may not damage the solution in particular simulations at operational resolution; however, they may later manifest themselves under unpredictable circumstances. Therefore, convergence testing is a valuable verification tool to build confidence in overall model performance.

Convergence testing is indeed commonly utilized for verification of the discretized model equations in the dynamical cores of atmospheric general circulation models (AGCMs) used in climate predictions (Rípodas et al., 2009; Stuhne & Peltier, 1999; Taylor et al., 1997). The same has not been true for physics parameterizations, where the verification of the discretized model equations is rarely completed in lieu of directing efforts instead towards the reformulation of the physics parameterizations. The motivation is typically that the error from the assumptions and simplifications is more significant than the error from the discretization. It is important to note that, as stated above, verification by convergence testing is less about decreasing discretization error and more about determining if the discrete model equations improperly represent the continuous model equations. Therefore, convergence test verification should be viewed not as a distraction from the reformulation of physics parameterizations, but instead as a way to ensure that the benefits of improved continuous model equations are realized in the corresponding discretized equations.

There is some momentum in utilizing convergence test verification to identify improperly discretized equations in physical parameterization (K. Zhang et al., 2012; Stinis et al., 2020; Wan et al., 2020; Vogl et al., 2020). Wan et al. (2020) identified improperly discretized equations using timestep convergence testing in a simplified atmospheric model that couples the dynamical core with a simplified parameterization for large-scale condensation processes. That result enabled improved discretization approaches in Wan et al. (2020) and Vogl et al. (2020) that enhance the trustworthiness of the physics parameterization as well as the weather and climate predictions from the AGCMs. Inspired by the success in those studies, this paper seeks to identify any improperly discretized equations in the Cloud Layers Unified by Binormals (CLUBB) model (Larson, 2017). Versions of CLUBB serve as the operational parameterization of clouds and turbulence in various AGCMs, including the Energy Exascale Earth System Model Atmosphere Model (EAM) (Xie et al., 2018; Rasch et al., 2019).

This paper begins by developing a convergence test environment for the CLUBB single-column model (CLUBB-SCM) that includes stratocumulus, two cumulus, and clear convective test cases. This environment is discussed in Section 2, followed by a discussion in Section 3 of modifications of CLUBB necessary to enable the convergence tests. Section 4 details the sources of pathologies identified both by convergence testing and the presence of nonphysical solution features. Suggested remedies to those pathologies are also presented. The impact of all suggested remedies on qualitative solution quality is discussed in Section 5. A summary of all conclusions and potential future work is found in Section 6.

2 Model and convergence testing

CLUBB is a unified parameterization of turbulence and cloud processes in the Earth's atmosphere (Larson, 2017). CLUBB contains 14 equations (c.f. the third column of Table A1) that prognose the grid-box mean state, turbulent fluxes, second- and third-order moments of vertical velocity(w), liquid water potential temperature (θ_l), total water mixing ratio (r_t), and horizontal winds (u and v). The dissipation and pressure terms in the prognostic equations are closed either by standard higher-order turbulence closures or by an assumption about the shape of the multivariate probability density function (PDF) of subgrid fluctuations in θ_l, r_t, and w (Golaz et al., 2002; Larson et al., 2007). The CLUBB-SCM solves these equations numerically over time for a one-dimensional vertical column. CLUBB's equations are discretized using semi-implicit time stepping and centered or upwind spatial differencing, which is expected to lead to an overall first-order accuracy in space and time. More details on CLUBB's equations and discretization can be found in Larson (2017).

Table 1. List of test cases for CLUBB-SCM used in this study

Cases	Long name	Regime	References
Wangara	Wangara Field Experiment	Dry convective boundary layer	Clarke (1971)
DYCOMS_RF02	Dynamics of Marine Stratocumulus	Stratocumulus cloud	Wyant et al. (2007) Stevens et al. (2003)
BOMEX	Barbados Oceanographic and Meteorological Experiment	Trade-wind cumulus under steady-state conditions	Holland and Rasmusson (1973) Siebesma et al. (2003)
RICO	Rain in Cumulus over the Ocean	Trade-wind cumulus and maritime shallow convection	Rauber et al. (2007) vanZanten et al. (2011)

In this study, we analyzed one stratocumulus case, two shallow-cumulus cases, and one dry turbulence case. Details for these cases can be found in Table 1 and the references therein. The configuration of CLUBB-SCM for each case is outlined in Table 2. The initial conditions and the atmospheric state at the surface (e.g. surface temperature and pressure) are prescribed using observed information from the appropriate field campaign (Table 1). The time-dependent surface moisture and heat fluxes from the large-eddy simulations (LES) are used to provide boundary conditions for Wangara, BOMEX and DYCOMS_RF02 cases, while the boundary conditions for RICO case is derived from a surface flux scheme (more discussion will be presented in Section 3). The large-scale dynamics, microphysics, and radiation are treated as forcing terms on the right-hand side of CLUBB's prognostic equations. The forcing of large-scale dynamics is prescribed, while, for simplicity, the forcing terms of microphysics and radiation are set to zero in the simulations discussed in Sections 3-4 by turning off the microphysics and radiation parameterizations. We note that if CLUBB were coupled to other parameterizations (e.g. radiation), then there would be effects on CLUBB's convergence properties, which is briefly discussed in Section 5

Table 2. List of configurations for CLUBB standalone model used in this study

Cases	initial conditions	boundary conditions	CLUBB configuration	other parameterizations	large-scale forcing
Wangara	prescribed sounding profile	prescribed time-dependent surface fluxes (Golaz et al., 2002)	Table A2	None	None
DYCOMS_RF02	case-specific (see Section 3)	prescribed time-dependent surface fluxes (Stevens et al., 2003)	Table A2	None	case-specific (Stevens et al., 2003)
BOMEX	prescribed sounding profle	prescribed time-dependent surface fluxes (Siebesma et al., 2003)	Table A2	None	case-specific (Siebesma et al., 2003)
RICO	prescribed sounding profle	case-specific time and resolution dependent surface fluxes (see Section 3)	Table A2	None	case-specific (vanZanten et al., 2011)

Our CLUBB-SCM simulations for each case were run on a stretched grid. The default setup for the model grid (referred to as Δz_0) is shown in Figure 1. The vertical resolution varies from 30m to 250m as one moves from the surface to the model top at around 10 km height (Figure 1). The grid type and resolution are similar to those for the lower-resolution configuration of the EAM model (see Figure 1 in Xie et al., 2018). The different levels of grid refinement with respect to the default grid in Figure 1 were used to construct space-time convergence test in this study. Specifically, a series of simulations were conducted by proportionally refining the vertical resolution (Δz) and model time step size (Δt) from (Δz_0, Δt_0) to (Δz_0, Δt_0)/ 2^7 in steps with a refinement factor of 2. Here, Δz_0 is the default model grid as shown in Figure 1, while $\Delta t_0 = 4$ s is selected to avoid the violation of the Courant–Friedrichs–Lewy (CFL) convergence condition for sim-

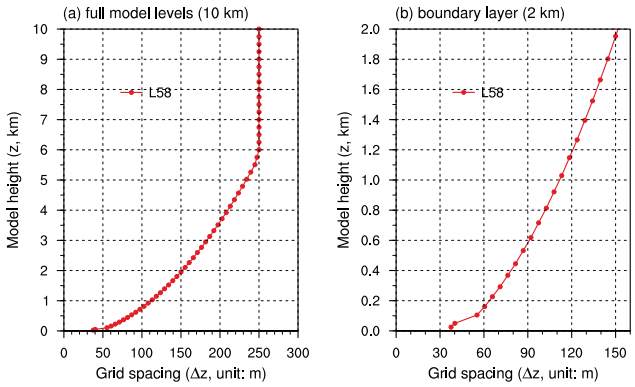

Figure 1. Reference vertical grid used for the test simulations with CLUBB-SCM. The total number of vertical levels is 58 (L58). The grid spacing varies from about 30 m near the surface to 250 m at the 6-km model height, while it is a constant of 250 m above 6-km model height. The grid type and resolution are similar to those in the lower-resolution configuration of E3SM model (see Figure 1 in Xie et al., 2018).

ulations with Δz_0. Also, Δt is refined such that $\frac{\Delta t}{\Delta z}$ in each grid cell remains constant (i.e. $\frac{\Delta t_0}{\Delta z_0}$) in order to avoid numerical instabilities associated with violation of the CFL condition. The simulation with (Δz_0, Δt_0)/ 2^7 in which the vertical resolution varies from 0.2 m to 2.0 m is used as the reference solution to evaluate the solution errors in the simulation with coarser resolutions and large time step sizes. For a physical quantity X in CLUBB at any time t, the average of root-mean-square solution error (RMSE) of the simulation with Δz is calculated with respect to the reference solution as:

$$\mathrm{RMSE(X, \Delta z)} = \left[\frac{\sum_{k=1}^{N} \left(X(k) - X_{ref}(k) \right)^2}{N} \right]^{\frac{1}{2}} \tag{1}$$

Where $X_{ref}(k)$ with a subscript ref denotes the value of X in layer k from the simulation with (Δz_0, Δt_0)/ 2^7. The convergence rate (order of convergence) p can be obtained from the slope of the curve of log(RMSE) versus log(Δz). In this study, as a constant grid refinement ratio (i.e. 2) is used, p is evaluated with

$$p = \frac{\log \left[\mathrm{RMSE(X, \Delta z_2)} - \mathrm{RMSE(X, \Delta z_1)} \right]}{\log(2)} \tag{2}$$

Where the RMSEs for Δz_1 and Δz_2 are derived from the simulations with (Δz_0, Δt_0)/ 2^5 and (Δz_0, Δt_0)/ 2^4, respectively.

The convergence rate p indicates how fast the computed solution converges to the reference solution or the true solution. Ideally, p will equal the order of accuracy for the discretization scheme, and recall that the expected value of p is 1 (i.e. first-order) for CLUBB-SCM. However, for the four cases with the default setups of CLUBB (first column in Table 1), the convergence tests (Figure 2) indicate that p values (numbers on the right corner of each panel) are less than 1 for the liquid water potential temperature (θ_l, panels a–d) and the third-order moment of vertical velocity ($\overline{w'^3}$) in most of the time periods during the 6-h simulation. The degradation of convergence is also observed in other prognostic variables (figures not shown). As will be discussed in the follow sections, the poor convergence are coincident with pathological behaviors of the discretized equations in CLUBB-SCM.

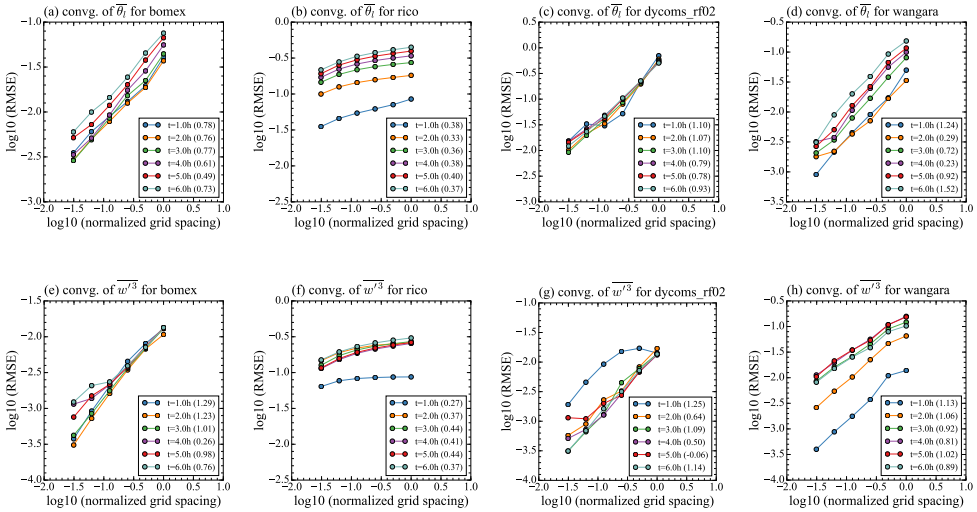

Figure 2. Space-time convergence with respect to the reference solution for liquid water potential temperature ($\overline{\theta_l}$, top row) and third-order moment of vertical velocity ($\overline{w'^3}$, bottom row) from the simulations for BOMEX (panels a and e), RICO (b,f), DYCOMS_RF02 (panels c and g), and Wangara (panels d andh) cases. The simulations were conducted with the default configuration in Table A2, in which the setups, including the initial and boundary conditions, follow the current operational CLUBB standalone model. To derive the convergence plot, simulations were run with various refinements of the vertical grid spacing and time step from the coarse values $(\Delta z_0, \Delta t_0)$ to values as fine $(\Delta z_0, \Delta t_0)/2^7$. The reference solution is derived from the simulation with $(\Delta z_0, \Delta t_0)/2^7$. The root-mean-square errors (RMSE) shown in the panels were calculated with respect to the reference solution following the method in Eq. (2). The convergence rates given in the parentheses are derived with Eq. (2). **We note that the desired first-order convergence is not usually achieved with CLUBB's default setups**.

3 Ensuring smooth initial conditions and grid-independent boundary conditions

In general, CLUBB's equations attempt to solve mixed initial boundary value problems. Table 3 lists the variables used in CLUBB's initial and boundary conditions to facilitate the discussion below.

The initial and boundary conditions in atmospheric models ought to be formulated properly in order to avoid unexpected effects on the numerical solution. For example, CLUBB parameterizes the surface fluxes for the RICO cumulus cloud case. The formulations for the surface fluxes can be written as:

$$\left[\overline{w'\theta_l'}\right]_{sfc} = -C_h||U||(\overline{\theta_l}_0 - \overline{\theta_l}|_{z=0}) \quad (3)$$

$$\left[\overline{w'r_t'}\right]_{sfc} = -C_q||U||(\overline{r_t}_0 - q_{sat}|_{z=0}) \quad (4)$$

$$\left[\overline{u'w'}\right]_{sfc} = -C_m||U||u_0 \quad (5)$$

$$\left[\overline{v'w'}\right]_{sfc} = -C_m||U||v_0, \quad (6)$$

where C_h, C_q, C_m, $||U||$, $\overline{\theta_l}|_{z=0}$ and $q_{sat}|_{z=0}$ denote the exchange coefficients of heat, moisture, momentum fluxes, mean wind speed, liquid water potential temperature, and saturation mixing ratio at the surface, respectively. The physical quantities $\overline{\theta_l}_0$, $\overline{r_t}_0$, u_0, and v_0 denote the liquid water potential temperature, total water mixing ratio, zonal and meridional wind components at the near-surface layer. Detailed descriptions can be found in Stevens et al. (2001) and vanZanten et al. (2011).

Table 3. List of variables in the initial and boundary conditions for CLUBB standalone model

Group name	Variables	Vertical levels
Initial condition	Liquid potential temperature ($\overline{\theta_l}$)	
	Total water ($\overline{r_t}$)	
	Zonal wind ($\overline{u}$)	All model levels
	Meridional wind ($\overline{v}$)	
	Vertical velocity wind ($\overline{w}$)	
Boundary condition	Heat flux ($[\overline{w'r_t'}]_{sfc}$)	
	Moisture flux ($[\overline{w'\theta_l'}]_{sfc}$)	Surface layer
	Momentum fluxes ($[\overline{u'w'}]_{sfc}$ and $[\overline{v'w'}]_{sfc}$)	

In the default setup for CLUBB, the bottom model level is treated as the near-surface layer to derive the surface fluxes. In this way, the surface fluxes are formulated in terms of model levels instead of physical altitude. To calculate the surface fluxes, the default vertical grid, as shown in Figure 1, CLUBB will use the near-surface quantities at 25 m. However, the near-surface level will be changed to 0.2 m when the resolution is refined by a factor of 2^7. This leads to an undesirable dependence of surface fluxes on the vertical resolution (c.f. Figure 3a for heat flux, and Figure B1 in appendix for momentum and moisture fluxes). As a result, the timing and the strength of the simulated clouds show substantial differences as the vertical resolution is refined (Fig. 3b–d). Because of this, the very poor convergence for RICO case (Figures 4a–b) are expected. Following these analyses, we revise the code to calculate the surface fluxes using the surface quantities at a fixed 20-m model level for all of the simulations, which reduces the dependence of the surface fluxes on the change of model resolution (Fig. 3e). As expected, the solution dependence on the change of model resolution are eliminated (Fig. 3f–h), and the solution convergence in RICO case are substantially improved (Fig. 4c–d).

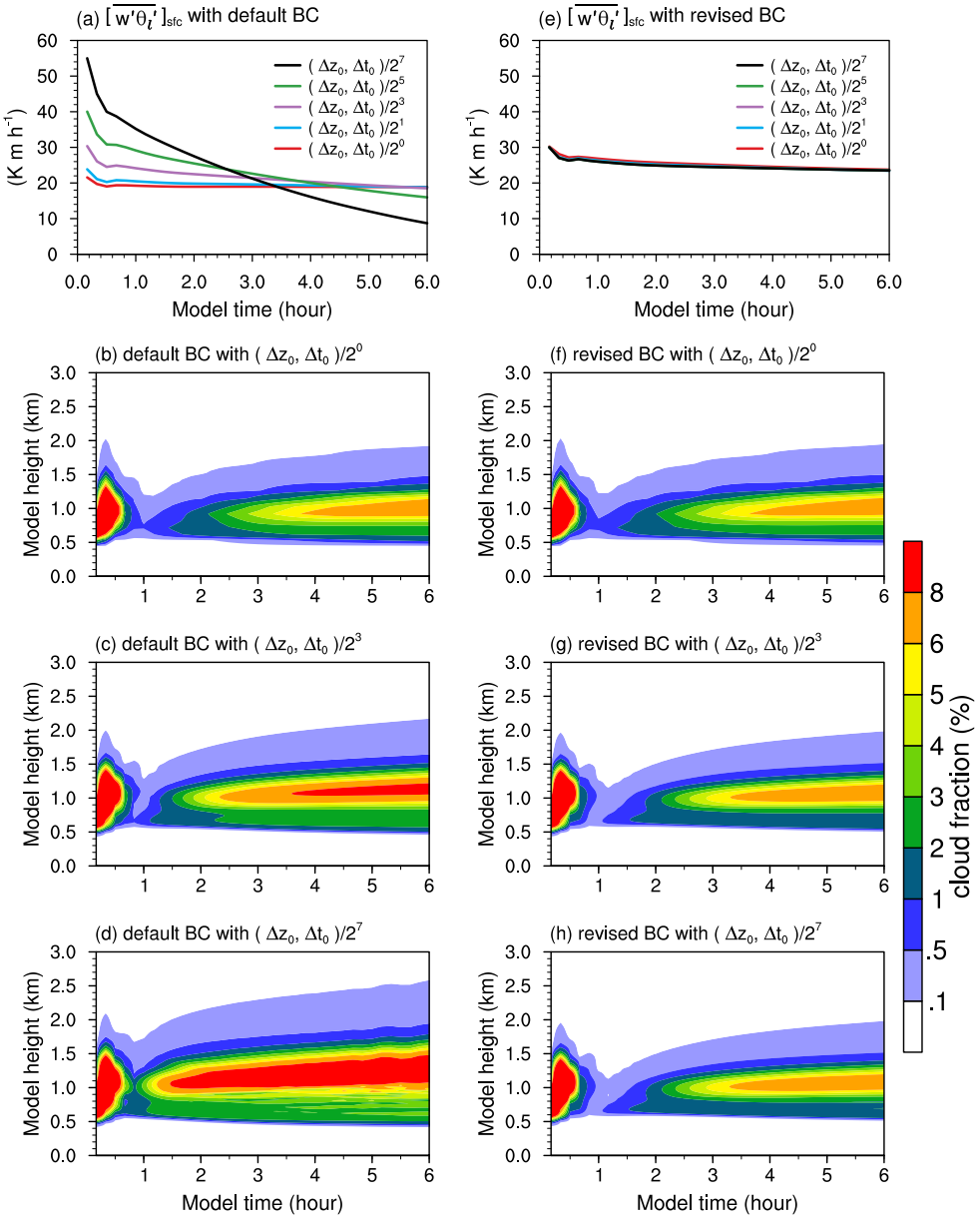

Figure 3. Time evolution of surface heat flux ($[\overline{w'\theta_l'}]_{sfc}$, unit: K m h^{-1}, first row), and Hovmöller diagram of cloud fraction (unit: %, second–fourth rows) in the simulations for the RICO cumulus cloud case during the 6-h period. The simulations were conducted with the default configuration in Table A2, except with "l_bc_at_constant height = .false." for the first column (panels a–d) and "l_bc_at_constant height = .true." for the second column (panels e–h). The former represents the default setup of surface fluxes in which the bottom model level changes with the resolution, while the latter represents the revised setup in which the surface fluxes are calculated at a constant model level located at 20 m. **With the default setup of boundary condition (BC) with grid-dependent surface fluxes (panel a), the cloud fraction evolves undesirably with increasing resolution (panels b–d).**

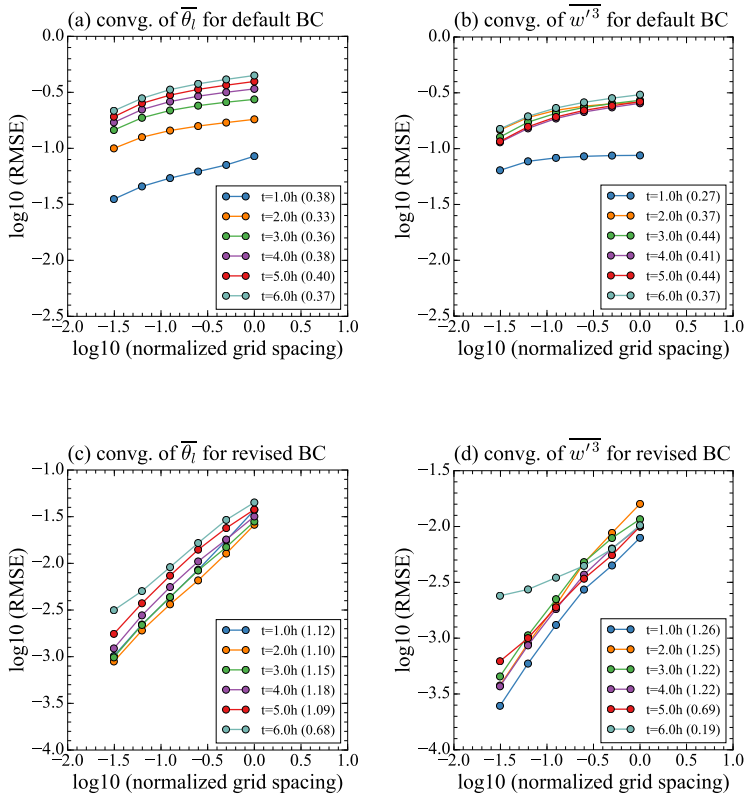

Figure 4. Space-time convergence with respect to the reference solution for liquid water potential temperature ($\overline{\theta_l}$, first column) and third-order moment of vertical velocity ($\overline{w'^3}$, second column) from the simulations for RICO cumulus cloud case. The simulations were conducted with the default configuration in Table A2, except with "l_bc_at_constant height = .false." for the first column (panels a–b) and "l_bc_at_constant height = .true." for the second column (panels c–d). The former represents the default setup of surface fluxes in which the bottom model level changes with the resolution, while the latter represents the revised setup in which the surface fluxes are calculated at a constant model level located at 20 m. The convergence test was conducted as in Figure 2, and the RMSE and convergence rates shown in this figure are defined as in Figure 2. **We note that the revised boundary condition (BC) lead to noticeable improvements of convergence in the RICO case (panels c–d) , as compared with the results for default setups (panels a–b)**.

A careful formulation of the initial condition is also important. For example, the initial state for DYCOMS_RF02 is idealized as a two-layer structure in liquid water potential temperature ($\overline{\theta_l}$, unit: K)and total-water specific humidity ($\overline{r_t}$, unit: g kg^{-1}) according to

$$\overline{\theta_l} = \begin{cases} 288.3 & z < z_i \\ 295 + (z - z_i)^{\frac{1}{3}} & z \geq z_i \end{cases} \tag{7}$$

$$\overline{r_t} = \begin{cases} 9.45 & z < z_i \\ 5 - 3\left(1 - e^{\frac{z - z_i}{500}}\right) & z \geq z_i. \end{cases} \tag{8}$$

Here z is model height, and z_i denotes the top of boundary layers where capping inversion happens in a stratocumulus cloud. Eqs. (7) and (8) were derived loosely from observations from the field campaign (Wyant et al., 2007).

Figure 5a shows the profiles of $\overline{\theta_l}$ for DYCOMS_RF02 from Eq.(7) with different vertical resolutions. The capping inversion is located at $z_i = 750$ m for this case. The inversion strength at $z = z_i$ in the simulations with default vertical resolution (i.e. Figure 1) is about 0.1 $K\ m^{-1}$, while it is increased to about 5 $K\ m^{-1}$ when the resolution is refined by a factor of 2^7 (Fig. 5b). The large gradient of $\overline{\theta_l}$ in the high-resolution simulations coincides with the formation of spikes in the turbulent advection of the third-order moments (i.e. $\overline{w'^3}$, Figure 5c).

The formation of spikes in the turbulent advection of $\overline{w'^3}$ (Fig. 5c) is likely unphysical because the sharp jump in temperature gradient at the inversion layer in Fig. 5a is not seen in the atmosphere. In addition, consider a centered finite difference approximation for the inversion strength at z_i from Eq. (7): $\frac{d\overline{\theta_l}}{dz} \approx \frac{288.3 - (295 + \Delta z^{1/3})}{2\Delta z}$. The value of this approximation will grow, without bound, like $-6.7/\Delta z$ with vertical grid refinement. Even worse, the centered finite difference approximation for $\frac{d^2\overline{\theta_l}}{dz^2}$ at z_i will grow like $-6.7/\Delta z^2$ with vertical grid refinement. Thus, the discontinuous initial conditions prescribed by Eq. (7) can invalidate the results of CLUBB's finite-difference discretization, and lead to the poor convergence seen in the dyncoms_rf02 case (Fig. 2c, g).

In this study, we addressed the issues in initial conditions for DYCOMS_RF02 case by reformulating Eq. (7) and Eq. (8) as:

$$\overline{\theta_l} = \begin{cases} 288.3 + H_\epsilon(z - z_i)\left(6.7 + \Delta z_0{}^{\frac{1}{3}}\right) & z - z_i < \Delta z_0 \\ 295 + (z - z_i)^{\frac{1}{3}} & z - z_i \geq \Delta z_0 \end{cases} \tag{9}$$

$$\overline{r_t} = \begin{cases} 9.45 - H_\epsilon(z - z_i)\left[4.45 + 3\left(1 - e^{\frac{\Delta z_0}{500}}\right)\right] & z - z_i < \Delta z_0 \\ 5 - 3\left(1 - e^{\frac{z - z_i}{500}}\right) & z - z_i \geq \Delta z_0. \end{cases} \tag{10}$$

Where Δz_0 is a constant of 20 m. $H_\epsilon(z - z_i)$ is a smoothed version of Heaviside function (Sussman et al., 1994; Lin et al., 2005) that smoothly varies from 0 to 1 in an interval of ϵ around $z = z_i$:

$$H_\epsilon(z - z_i) = \begin{cases} 0 & z - z_i < -\epsilon \\ \frac{1}{2}\left[1 + \frac{\mathrm{z - z_i}}{\epsilon} + \frac{1}{\pi}\sin\left(\frac{\mathrm{z - z_i}}{\epsilon}\pi\right)\right] & |z - z_i| \leq \epsilon \\ 1 & z - z_i > \epsilon, \end{cases} \tag{11}$$

The smoothed Heaviside does not introduce jumps from 0 and 1 when $z = z_i$, as compared with the results from the standard definition of the Heaviside:

$$H(z - z_i) = \begin{cases} 0 & z - z_i < 0 \\ 1 & z - z_i \geq 0. \end{cases} \tag{12}$$

Figures 5d-f illustrate the results from the simulations that are initialized with the profiles from Eq. (9) and Eq. (10). Here, $\epsilon = \Delta z_0 = 20\ m$ is selected empirically for

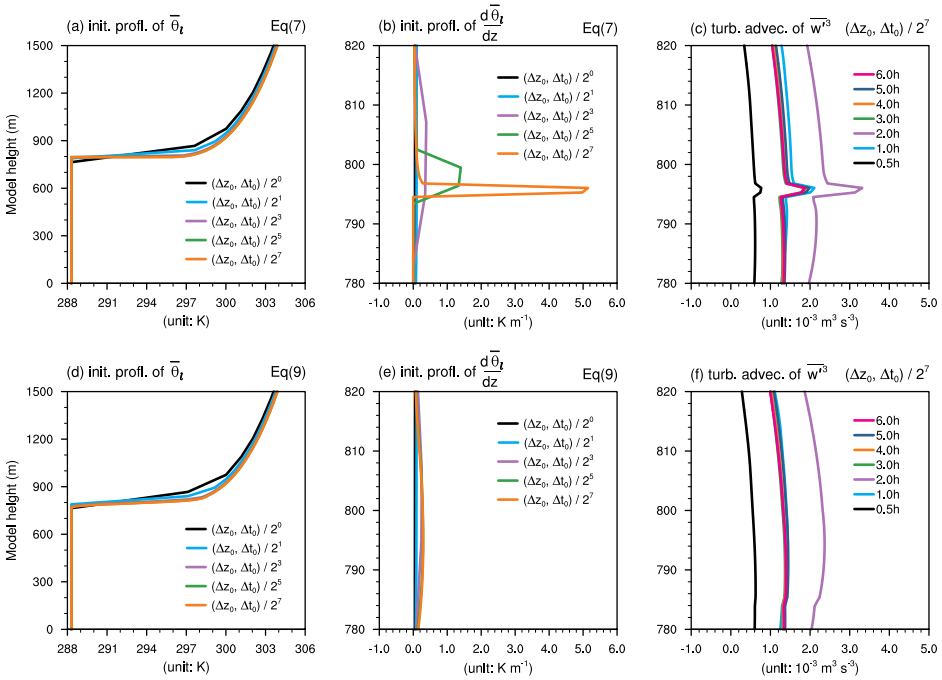

Figure 5. Initial profile of liquid water potential temperature ($\overline{\theta_l}$, panels a and d); the vertical gradient of $\overline{\theta_l}$ ($\frac{d\overline{\theta_l}}{dz}$, panels b and e); and turbulent advection of $\overline{w'^3}$ (panels c and f) from the simulations for DYCOMS_RF02 stratocumulus cloud case. The simulations were conducted with the default configuration in Table A2, except with "l_new_dycoms2_sounding = .false." for the first row (panels a–c), while "l_new_dycoms2_sounding = .true." for the second row (panels d–f). The former represents the default setup that initializes $\overline{\theta_l}$ using Equation (7), while the latter represent the revised setup that initializes $\overline{\theta_l}$ using Equation (9). Various refinements of the vertical grid are shown in the first two columns, and the finest refinement with $(\Delta z_0, \Delta t_0)/2^7$ at various times is shown in the third column. **The default initialization of $\overline{\theta_l}$ for DYCOMS_RF02 causes strong dependence of $\partial\overline{\theta_l}/\partial z$ on vertical resolution, which leads to the formation of spikes near the inversion in panels b–c.**

the smoothed Heaviside function in all simulations. We can see that the initial profile of $\overline{\theta_l}$ in Fig. 5d is still very close to that in Fig. 5a; however, the simulations of DYCOMS_RF02 show smoothed profiles of $\frac{d\overline{\theta_l}}{dz}$ (Fig. 5e) and the turbulent advection of $\overline{w'^3}$ (Fig. 5f).

We point out that the interpolation method for the remapping of the coarser-resolution sounding profile to the finer-resolution model grid can also invalidate the result of finite difference schemes. For instance, linear interpolation only ensures the C^0 continuous (the interpolated variable itself is continuous in space and time), which can result in unbounded derivatives. In this scenario, a high-order interpolation method such as cubic spline can be a better choice to reduce the impact of interpolation on the initial condition. As we found in this study, the solution convergence of $\overline{\theta_l}$ (Fig. 6a) and $\overline{r_t}$ (Fig. 6b) at hour 1 in the BOMEX case is restored to the expected first order when we changed the linear interpolation (blue lines) to cubic-spline interpolation (orange lines). In addition, the configuration with all the revisions in the initial and boundary conditions are used as the baseline (referred to as "baseline configuration" in Table A2) to discuss the problems in CLUBB's discretized equations. Figure B2 in appendix shows the space-time convergence of $\overline{\theta_l}$ and $\overline{w'^3}$ from the simulations with the baseline configuration; and the expected first-order convergence in these quantities are still not achieved in most of time for the four cases.

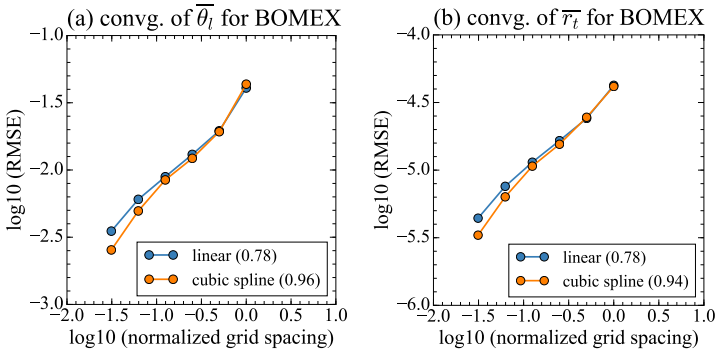

Figure 6. Space-time convergence with respect to the reference solution for (a) liquid water potential temperature ($\overline{\theta_l}$), and (b) total water mixing ratio ($\overline{r_t}$) at hour 1 in the BOMEX cumulus cloud case. The simulations were conducted with the default configuration in Table A2 with linear interpolation (blue lines) and cubic spine interpolation (orange lines) for the remapping of the coarser-resolution sounding profile to the finer-resolution model grid, respectively. The convergence test was conducted as in Figure 2, and the RMSE and convergence rates shown in this figure are defined as in Figure 2. **We note that the cubic spine interpolation (orange lines) leads to noticeable improvements of convergence in the BOMEX cases in the first hour simulation, as compared with the results from linear interpolation (blue lines)**.

4 Causes of nonphysical features and degradation of convergence

Apart from the initial and boundary conditions, problems in CLUBB's discretized equations themselves are found to result in nonphysical features and, consequently, degradation of convergence. Two aspects of defects in CLUBB equations are identified and discussed in this section. First, limiters used in CLUBB's dissipation time scale with the intention of keeping certain quantities bounded are found to have unintentional effects on solution profiles. Second, CLUBB's formulation of dissipation terms is found to add

to nonphysical oscillations and gradients instead of decreasing or smoothing such features. Because CLUBB's use of limiters and formulation of dissipation terms is common to other parameterizations, the lessons learned herein are important for the wider parameterization community.

4.1 Limiters and discontinuities

The CLUBB moisture flux equation (i.e. $\overline{w'r_t'}$) has the following turbulent sink:

$$\frac{\partial \overline{w'r_t'}}{\partial t} = ... + \frac{C}{\tau}\overline{w'r_t'}, \tag{13}$$

where C is tunable parameter and τ is an eddy turnover timescale. That timescale is formulated as (Guo et al., 2021)

$$\frac{1}{\tau} = \left[C_0\frac{1}{\tau_0} + C_1\sqrt{\left(\frac{\partial u}{\partial z}\right)^2 + \left(\frac{\partial v}{\partial z}\right)^2} + C_3\sqrt{N^2}\right]\left[1 + H(N^2 - N_0^2)C_4\sqrt{R_i}\right], \tag{14}$$

where C_i and τ_0 are constants and N^2 denotes the Brunt-Väisälä frequency, which measures the stability of atmospheric flow. CLUBB approximates N^2 as

$$N^2 = \frac{g}{\overline{\theta_l}}\frac{d\overline{\theta_l}}{dz}, \tag{15}$$

where $\overline{\theta_l}$ is the liquid water potential temperature and g is the gravitational acceleration. The $H(N^2 - N_0^2)$ term is a Heaviside function Eq. 12 that activates when N^2 is greater than a threshold value N_0^2. The quantity R_i denotes the Richardson number, which is an index of stability and is defined as the square of the ratio of Brunt-Väisälä frequency to the shear production of turbulence (the generation of turbulence kinetic energy caused by wind shear). It is implemented in CLUBB as

$$R_i = \frac{\min\{N^2, N_{max}\}}{\max\left\{\left[\left(\frac{\partial u}{\partial z}\right)^2 + \left(\frac{\partial v}{\partial z}\right)^2\right], f_{min}\right\}}, \tag{16}$$

where R_i is limited by the minimum function in numerator and the maximum function in the denominator. In the default setup of CLUBB, f_{min} is set to a constant value of $1E-7$, and N_{max} is empirically defineed as $N_{max} = |N^2|^3 \times 1E8$.

Limiters with minimum and maximum functions

Limiters with minimum and maximum functions such as those in Eq. (16) are frequently seen in the physics parameterizations for AGCMs. While such limiters are typically meant to clip the numerical solution back to physical values (e.g., clipping a slightly negative density back to zero), they can also push the numerical solution to nonphysical profiles. As an example, Figure 7 shows the profiles of the R_i at the end of a 5-h model integration for the BOMEX and DYCOMS_RF02 cases. The profiles with the N_{max} limiter show the sawtooth-shaped oscillation of R_i seen at the 500-1000m region in BOMEX case and the non-smoothness of R_i seen at the 400-800m region in the DYCOMS_RF02 case. The numerical solutions without the N_{max} limiter exhibit smoother, more physical profiles.

We note that the nonphysical features in R_i will feed into the prognostic equations of $\overline{w'r_t'}$ via Eq. (14) and Eq. (13). Indeed, the formation of nonphysical sawtooth-shaped oscillation coincides with poor convergence of $\overline{w'r_t'}$ in the four cases with different cloud regimes shown in Fig. 8. The convergence of all cases improves at least somewhat when the N_{max} limiter in the numerator term is removed from Eq. (16). In this study, we remove the limiter N_{max} from Eq. (16) in order to eliminate its impact on R_i and the model

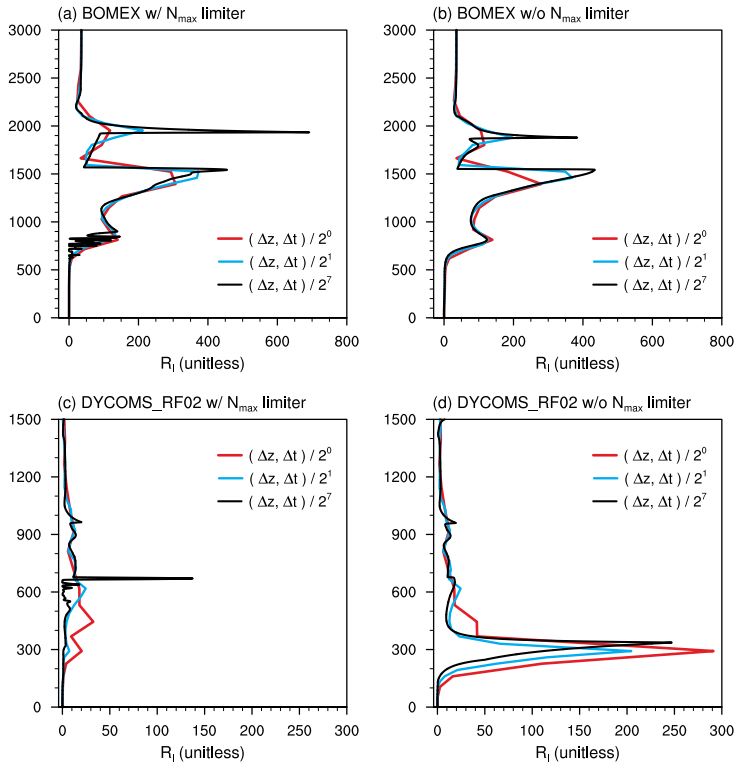

Figure 7. Profiles of Richardson number (R_i, unitless) from the simulation for BOMEX cumulus cloud (first row) and DYCOMS_RF02 stratocumulus cloud (second row) cases. The instantaneous model output at the end of hour 5 is plotted. The simulations were conducted with baseline configuration in Table A2, except with "l_bvf_max_limiter = .true." for the first column (panels a and c), while "l_bvf_max_limiter = .false" for the second column (panels b and d). The former represents the default setup with N_{max} limiter in Eq. (16), while the latter represents the revised setup that turns off N_{max} limiter in Eq. (16). **The use of the N_{max} limiter leads to non-smoothness (i.e. sawtooth-shaped oscillations) of R_i at 400-800m region in BOMEX case (panel a versus panel b) and at 600-700m region in DYCOMS_RF02 case (panel c versus panel d).**

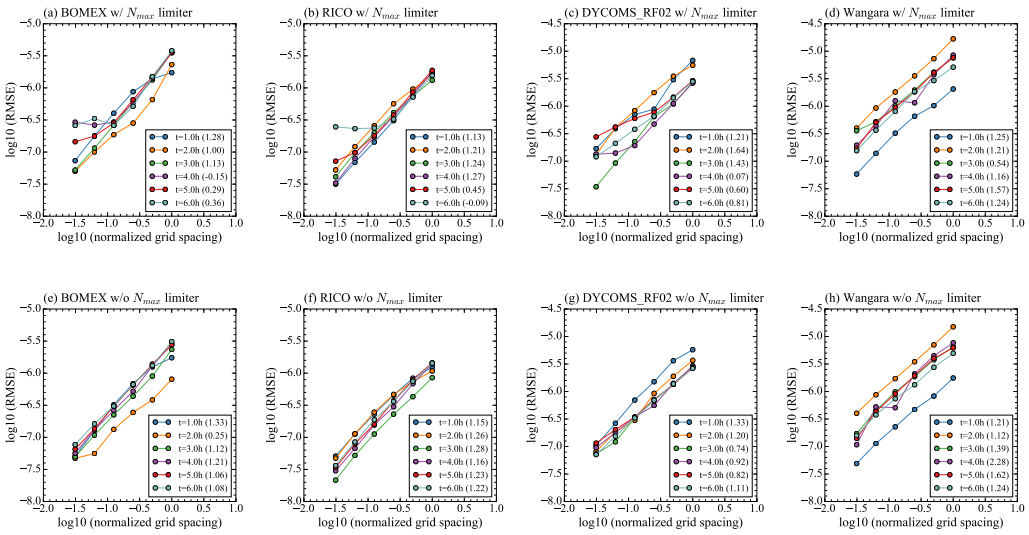

Figure 8. Space-time convergence with respect to the reference solution for turbulence moisture flux ($\overline{w'r'_t}$) from the simulation for BOMEX (first column), RICO (second column), DYCOMS_RF02 (third column) and Wangara (fourth column) cases. The simulations were conducted with the baseline configuration in Table A2, except with "l_bvf_max_limiter = .true." for the first row (panels a–d), while "l_bvf_max_limiter = .false." for the second row (panels e–h). The former represents the default setup with N_{max} limiter in Eq. (16), while the latter represents the revised setup that turns off N_{max} limiter in Eq. (16). The convergence test was conducted as in Figure 2, and the RMSE and convergence rates shown in this figure are defined as in Figure 2. **We note that the revised setups without the N_{max} limiter substantially improves the solution convergence in all four cases**.

solution of CLUBB:

$$R_i = \frac{N^2}{\max\left\{\left[\left(\frac{\partial u}{\partial z}\right)^2 + \left(\frac{\partial v}{\partial z}\right)^2\right], f_{min}\right\}}. \tag{17}$$

We simply remove it because the N_{max} limiter has little theoretical justification and provides relatively little benefit in global simulations. However, if retaining the N_{max} limiter is desired, one could attempt to smooth the corresponding minimum function. We have not explored that option here.

Discontinuities in formulation

Sharp changes in terms, such as the Heaviside function in Eq. (14), are also frequently seen in the physics parameterizations for AGCMs. The Heaviside function $H(N^2-N_0^2)$ is used to apply an amplification factor to $\frac{1}{\tau}$ when N^2 is greater than N_0^2. We note that this function, defined as in Eq. 12, jumps from 0 and 1 wherever $N^2 = N_0^2$ ($3.3E-4$ in the default setup of CLUBB), which introduces jumps in $1/\tau$ or one of its derivatives. Such jumps may be not only nonphysical, but they can also invalidate the use of finite-difference approximations for spatial derivatives. Even if there is no spatial derivative where the jump is introduced, as is the case with Eq. (13), the jumps can propagate through the prognostic equations to a spatial derivative elsewhere in the equation set, leading to nonphysical solution profiles. A smoothed version of Heaviside formulated as in Eq. (11) is a commonly used alternative to the standard Heaviside. As mentioned in Section 3, the magnitude of the smoothing parameter $\epsilon > 0$ needs to be determined. For the problem discussed here, the value of ϵ is restricted to values less than N_0^2 in order to prevent the amplification factor to $1/\tau$ from being applied when $N^2 < 0$.

Figure 9 shows the profiles of N^2, the standard Heaviside function (12), the smoothed Heaviside function (11) with $\epsilon = 0.1N_0^2 = 3.3E-5$, and $1/\tau$ at the end of 3-h simulations of DYCOMS_RF02 case. We can see that the Heaviside functions are triggered within the 500-1200m region (Fig. 9b) as $N^2 > N_0^2$ (Fig. 9a). The sharp transition from 0 to 1 for $H(N^2-N_0^2)$ happens at cloud bottom (around 600m) and cloud top (around 950m) (Fig. 9b), which accounts for the formation of a jump and nonphysical overshoot in the vertical profile of $\frac{1}{\tau}$ at around 950m in the high-resolution simulations (black line, Fig. 9c). The profiles of $H_\epsilon(N^2 - N_0^2)$ generated with Eq. (11) show overall similar shape as in Fig. 9b; however, the small overshoot at 950 m in $\frac{1}{\tau}$ shown in Fig. 9c is effectively eliminated by using smoothed Heaviside function (Fig. 9f). The use of the smoothed Heaviside function H_ϵ instead of H also coincides with the restoration of first-order convergence of $\overline{w'r_t'}$ in the BOMEX, DYCOMS_RF02, and Wangara cases (comparing Fig. 10 with Fig. 8e-h). We note that the smoothed Heaviside might be generally considered as a replacement for problematic Heaviside functions provided the value for ϵ can be determined from physical intuition.

4.2 Improper treatment of dissipation terms

Background eddy diffusion was introduced into the CLUBB equations not to represent the physical transport of fluxes but rather to provide numerical smoothing (Larson, 2017). The corresponding terms are of the form

$$\frac{\partial \overline{X}}{dt} = \underbrace{\frac{1}{\rho}\frac{\partial}{\partial z}\left(\rho K \frac{\partial \overline{X}}{dz}\right)}_{\text{diffusion}}, \tag{18}$$

where $\overline{X}$ denotes the high-order moments in CLUBB parameterization, K is the diffusion coefficient that typically depend on $\overline{X}$, and ρ is air density.

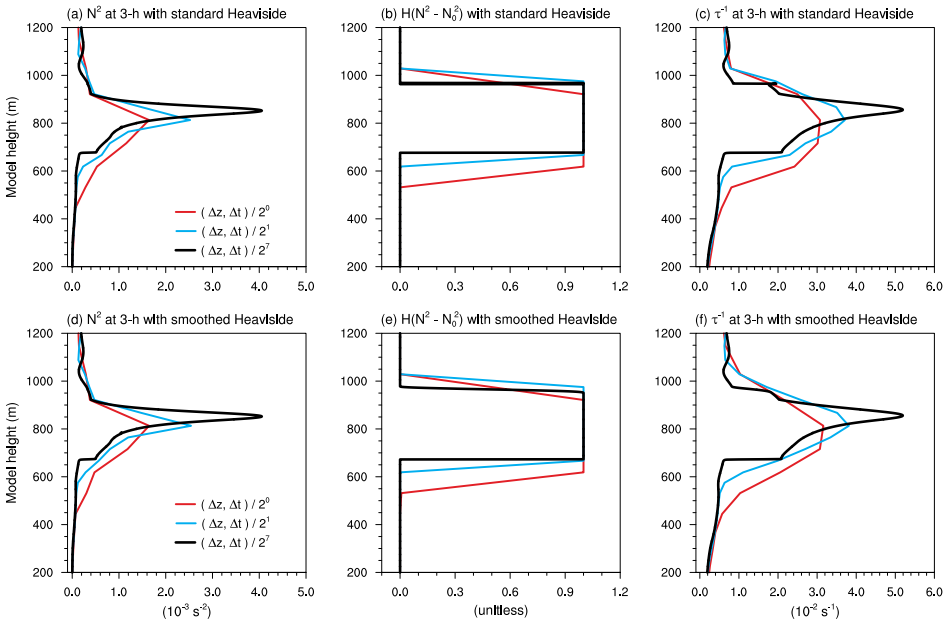

Figure 9. Profiles of the Brunt-Väisälä frequency (N^2, unit: s^{-2}, first column), Heaviside function ($H(N^2\text{-}N_0^2)$, unitless, second column) and inverse of eddy turnover time scale ($\frac{1}{\tau}$, unit: s^{-1}, third column) from the simulations for DYCOMS_RF02 stratocumulus cloud case. The instantaneous model output at the end of hour 3 is used to derive the plots. The simulations were conducted using "l_smth_Heaviside_tau_wpxp = .false." for the top row (panels a–c) and "l_smth_Heaviside_tau_wpxp = .true." for the bottom row (panels d–f), with all other configuration values from baseline configuration in Table A2 except with "l_bvf_max_limiter = .false". The former represents the default setup with the unsmoothed Heaviside function of Eq. (12), while the latter represents the revised setup with the smoothed Heaviside function of Eq. (11). **Smoothing the Heaviside function as in Eq. (11) leads to smoother profiles of $\frac{1}{\tau}$ in the bottom row (panel f versus panel c at around 950 m)**.

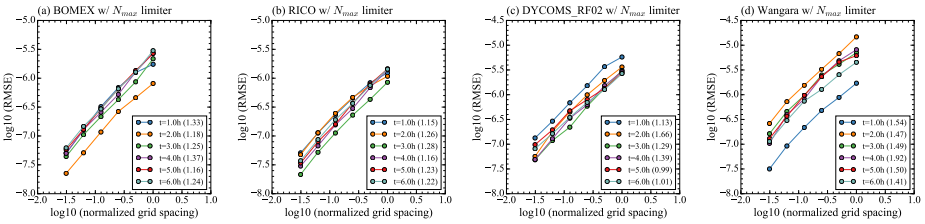

Figure 10. Space-time convergence with respect to the reference solution for turbulence moisture flux ($\overline{w'r_t'}$) from the simulation for (a) BOMEX, (b) RICO, (c) DYCOMS_RF02 and (d) Wangara cases. The simulations were conducted with the baseline configuration in Table A2, except with "l_bvf_max_limiter = .false." and "l_smth_Heaviside_tau_wpxp = .true.". In contrast with the model setups in Fig. 8e–h, the configuration here uses the smoothed Heaviside function of Eq. (11). The convergence test was conducted as in Figure 2, and the RMSE and convergence rates shown in this figure are defined as in Figure 2. **Smoothing the Heaviside function as in Eq. (11) leads to the expected first-order convergence in BOMEX, DYCOMS_RF02 and Wangara cases**.

To better understand the behavior of Eq. (18), it can be rewritten as

$$\frac{\partial \overline{X}}{dt} = \underbrace{K\frac{\partial^2 \overline{X}}{dz^2}}_{\text{dissipation}} + \underbrace{\frac{1}{\rho}\frac{\partial \rho K}{\partial z}\frac{\partial \overline{X}}{dz}}_{\text{advection}}. \tag{19}$$

In this way, the diffusion can be separated into a dissipation component (as $K \geq 0$) and an advection component with advection velocity $\frac{\partial \rho K}{\partial z}$. The dissipation component will damp spatial oscillations with a strength proportional to the frequency of the oscillation. The advection component will either compress and extend spatial oscillations depending on the profile of the advection velocity. Therefore, the advection component can actually *sharpen* features that perhaps the eddy diffusion term was intended to smooth.

Figure 11 shows the profiles of $\overline{w'^3}$ and K in the BOMEX cumulus cloud case both using the full numerical diffusion (18) and using just the dissipation term in (19). Note

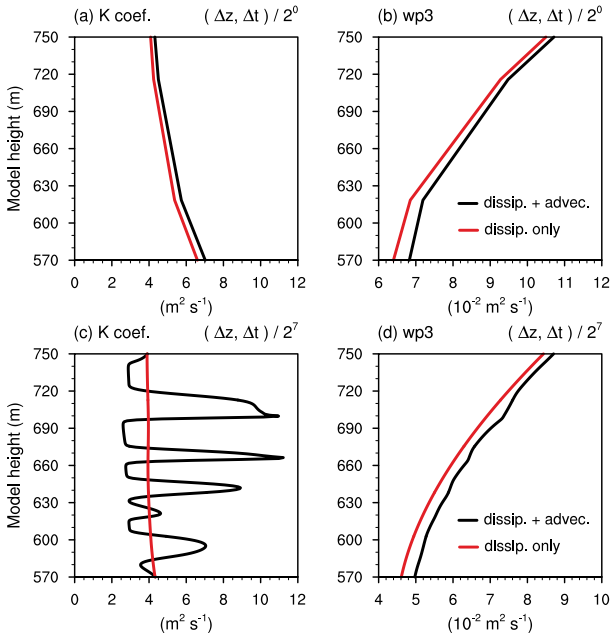

Figure 11. Profiles of non-linear diffusion coefficient (K, unit: $m^2\ s^{-1}$, panels a and c), and the third-order moment of vertical velocity ($\overline{w'^3}$, unit: $m^3 s^{-3}$, panels b and d) from the simulation for BOMEX cumulus cloud case. The instantaneous model output at hour 4 of the simulation with the finest resolution (first row) and the coarsest resolution (second row) are used to derive the plots. The simulations were conducted with the baseline configuration in Table A2, except with "l_pure_diffusion = .false." for the black lines, while "l_pure_diffusion = .true." for the red lines. The former represents the default setup with diffusion formulated as in Eq. (18), while the latter represents the revised setup by change the diffusion to dissipation formulated as the first righthand term in Eq. (19). **Changing the diffusion to dissipation eliminate the unphysical sawtooth-shaped oscillation in the non-linear diffusion coefficients K and $\overline{w'^3}$ caused by numerical diffusion (panels e–h versus panels a–d).**

the appearance of nonphysical, small-scale features in the high resolution solutions when the full numerical diffusion is used. Such small-scale features are not seen when only dissipation is used. Additionally, the profile for K identifies multiple regions where the ad-

vection component will be compressing features (regions of positive slope below negative slope). Note that the coarser resolution solutions do not show the same formation of nonphysical small-scale features, because the coarser resolution cannot resolve such scale lengths. That said, the introduction of nonphysical features to the model equations at any scale should be avoided.

Figure 12 shows the effects of the formation of the nonphysical features on the convergence of $\overline{w'^3}$. Note the degradation in convergence in the solution after 4 hours and after 6 hours is consistent with unresolved, small-scale features in the model equations. The use of the dissipation in Eq. (19) instead of the diffusion in Eq. (18) is found to avoid nonphysical, small-scale features, as well as the convergence issues they can cause, in other cases as well. With these findings, we believe that the dissipation term in Eq. (19) would be a better choice to fulfill the purpose of eddy diffusion in CLUBB, namely to stabilize the numerical solutions. In many models, eddy diffusivity is used not merely to smooth solutions but also to parameterize fluxes (e.g. Holtslag & Moeng, 1991; Stevens, 2000; Nakamura, 2001; Siebesma et al., 2007; Suselj et al., 2019). In those models, one cannot simply delete the advection term. However, preventing the advection from introducing sawtooth noise is a problem that is beyond the scope of this paper.

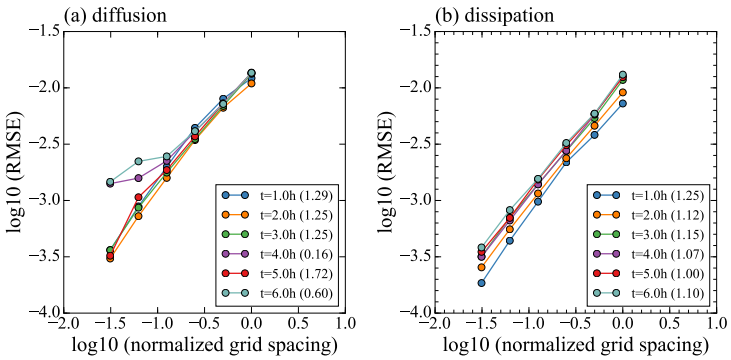

Figure 12. Space-time convergence with respect to the reference solution for the third-order moment of vertical velocity ($\overline{w'^3}$) from the simulation for the BOMEX cumulus cloud case. The simulations were conducted with the baseline configuration in Table A2, except with " l_pure_diffusion = .false." for panel (a) and "l_pure_diffusion = .true." for panel (b). The former represents the default setup with diffusion formulated as in Eq. (18), while the latter represents the revised setup by changing the diffusion to dissipation formulated as the first right-hand term in Eq. (19). The convergence test was conducted as in Figure 2, and the RMSE and convergence rates shown in this figure are defined as in Figure 2. **Changing the diffusion to dissipation restores the expected first-order convergence of $\overline{w'^3}$ during the hour 4 to hour 6 period in panel (b) for BOMEX case**.

5 Comparison of Solutions from Revised and Baseline CLUBB

In this section, we compare the solutions from CLUBB that are produced with the baseline and revised configurations listed in Table A2. The baseline configuration largely follows the default setups in the current operational CLUBB except that initial and boundary conditions are revised as described in Section 3. This is done to avoid the strong dependence of the solution on the initial and boundary conditions and thereby focus on the discretization of CLUBB's prognostic equations themselves. In contrast to the baseline configuration, the revised configuration contains all the code changes that are pro-

posed in Section 4 to eliminate the unphysical oscillations, as well as restoring convergence.

To observe whether the reference solution or physical processes in CLUBB are significantly different, Figure 13 shows the Hovmöller diagrams of cloud fraction field in the simulations for BOMEX, RICO, and DYCOMS_RF02 case with the finest resolution (i.e. refining of the vertical resolution and model time step by a factor of 2^7). The development and the structure of the cumulus (BOMEX and RICO) and stratocumulus (DYCOMS_RF02) cloud are still well captured by the revised configuration (Fig. 13d-f) compared to the baseline configuration (Fig. 13a-c). The intensity of the cloud (magnitude of cloud fraction) in three cases with revised configuration is also similar to those in the baseline configuration, except that the revised configuration produces about 2% reduction of cloud fraction in RICO case at around 1 km region (Fig. 13b versus Fig. 13e). The simulated features of physical quantities (e.g. $\overline{w'^3}$) in the dry turbulence case (i.e. Wangara) were also checked (Fig B4), and we conclude that the revised configuration overall produces qualitatively similar solutions compared to the baseline configuration in all four cases.

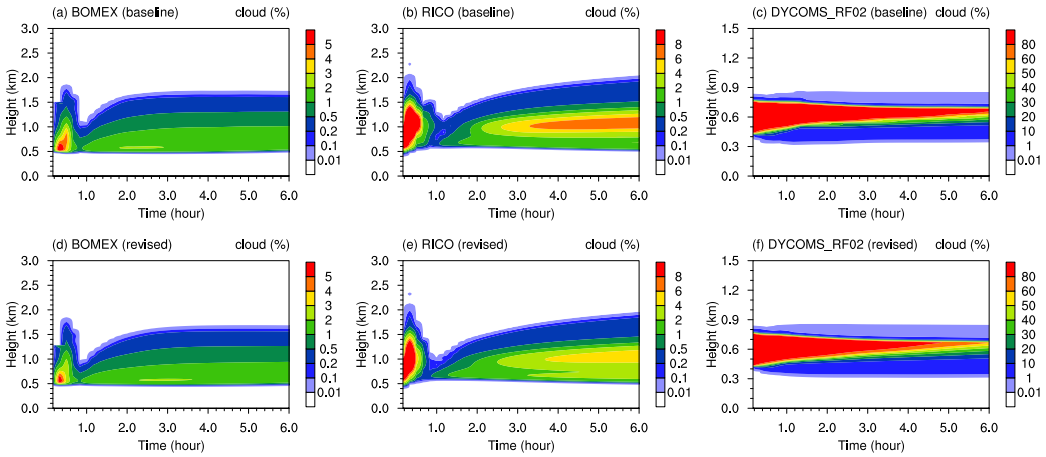

Figure 13. Hovmöller diagrams of cloud fraction (unit: %, first column) and turbulence length scale (unit: m, second column) from the simulation for BOMEX cumulus cloud case. The simulations were conducted with $(\Delta z_0, \Delta t_0)/2^7$ using the baseline configuration for the first row (panels a–c), and the revised configuration for the second row (panels d–f). The details of baseline and revised configuration can be found in Table A2. Δz_0 is the reference model grid in Fig 1, and $\Delta t_0 = 4$ s. **We note that the development of cloud in three cases is qualitatively similar in the simulations with baseline and revised configurations**.

The revised configuration eliminates the unphysical oscillations in high-resolution simulations, enhancing our confidence in the trustworthiness of solutions from CLUBB. Figure 14 shows the Hovmöller diagrams of turbulence length scale (L_{scale}) field in the simulations for the three cases in Fig. 13. Here, L_{scale} is derived from the eddy turnover time scale τ discussed in Section 4.1 and the turbulence kinetic energy, which can be used to reveal the quality of solutions from CLUBB's prognostic equation. As shown in Fig. 14a-b, oscillatory features in L_{scale} were pronounced at 0.5–1.0 km region in the simulation with baseline configuration for BOMEX (after 3–h in Fig. 14a) and RICO (after 4–h in Fig. 14b). As the vertical resolution and model time step in this simulation is sufficiently small, smoother temporal and spatial variations in the physical quantities are expected. The oscillatory features in L_{scale} are likely unphysical by intuition. With the revised con-

figuration, the unphysical oscillations of L_{scale} are not seen in the simulations for BOMEX and RICO cases (Fig. 14d-e). In addition, smoother vertical variation of L_{scale} are also achieved by the revised configuration in DYCOMS_RF02 case. The periodical appearance of local maxima within 0.5–0.7 km region during 2–6 h period in Fig. 14c are eliminated with the revised configuration (Fig. 14e).

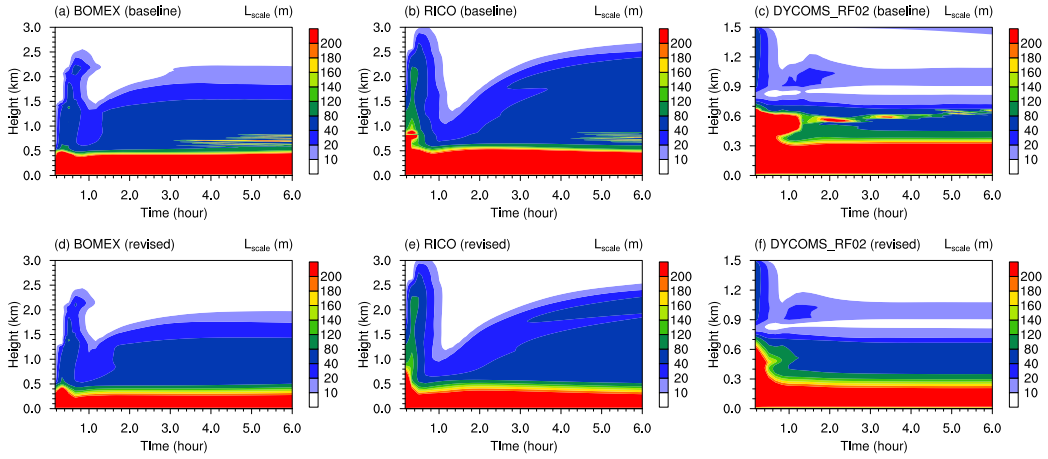

Figure 14. As in Figure 13 but showing Hovmöller diagrams of turbulence length scale (L_{scale}, unit: m) from the simulations with baseline (first row) and revised (second row) configurations in Table A2, respectively. **With the revised configuration, the development of unphysical oscillations in L_{scale} in the simulations with baseline configuration are effectively mitigated**.

The revised configuration that eliminates the unphysical oscillations of the solution from CLUBB (see Section 4) leads to the restoration of the expected first-order convergence in the four cases with different cloud regimes, as compared with the results from the baseline configuration. This is evidenced in Fig. 15 for the third order moments of vertical velocity ($\overline{w'^3}$) and Figure B5 in the appendix for the liquid potential temperature ($\overline{\theta_l}$). The expected first-order convergence in the revised configuration increases our confidence in the model fidelity and trustworthiness.

CLUBB is typically limited to using a larger time step size in practical implementations because of computational cost restrictions, despite the consequent loss in accuracy. We discover that the improved discretization in CLUBB that address the unphysical oscillations and improve the solution convergence in high-resolution simulations can be also beneficial for the simulations with large time step sizes. Figure 16 compares the 6-h mean profile of the third-order moments of vertical velocity ($\overline{w'^3}$) from the simulations with three different resolutions using baseline and revised configurations in Table A2. The black lines denote the high-resolution simulation (labeled as "reference") that refine the reference model grid (Fig. 1a) and time step size (4 s) by 2^7. The colored lines represent the simulations using the reference model grid with 300 s ($\Delta t = 300$ s, red lines) and 600 s ($\Delta t = 600$ s, blue lines) time steps (Δt) . The $\Delta t = 300$ s simulation closely represents the operational configuration of CLUBB in the EAM model. Compared to the baseline configuration (Fig. 16a-d), the revised configuration improves the agreement between the simulations with lower spatial and temporal resolutions (blue and red lines) and the reference solution (black lines) with high spatial and temporal resolution (Fig. 16e-h). Other physical quantities are also checked, and we found that significant improvements are observed in most of the physical quantities for BOMEX (Fig. B6 in appendix)

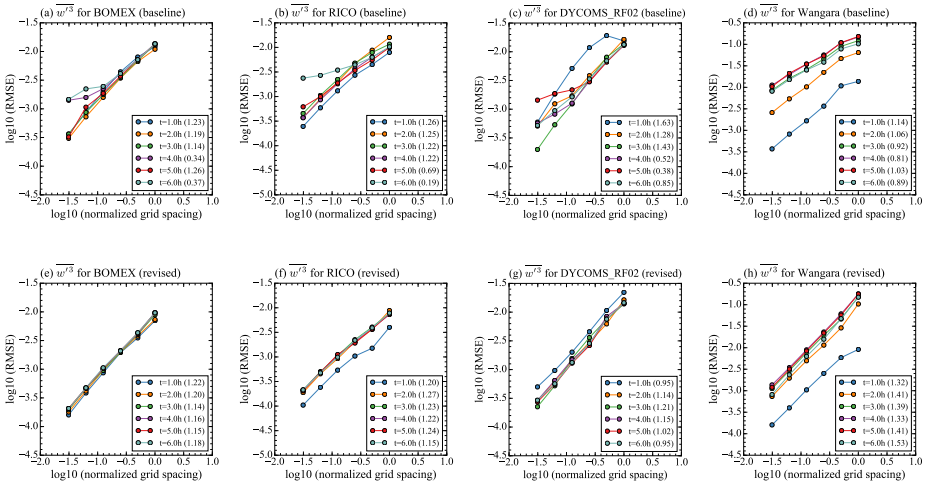

Figure 15. Space-time convergence with respect to the reference solution for the third-order moment of vertical velocity ($\overline{w'^3}$) from the simulations for BOMEX (panels a and e), RICO (panels b and f), DYCOMS_RF02 (panels c and g), and Wangara (panels d and h). The simulations were conducted with the baseline configuration for the first row (panels a–d), and the revised configuration for the second row (panels e–h) in Table A2. The revised configuration combines all the changes in CLUBB discussed in Section 4. The convergence test was conducted as in Figure 2, and the RMSE and convergence rates shown in this figure are defined as in Figure 2.**Compared to the baseline configuration (panels a–d), the revised configuration with the proposed code changes in CLUBB restores the expected first-order convergence in all four cases (panels e–h)**.

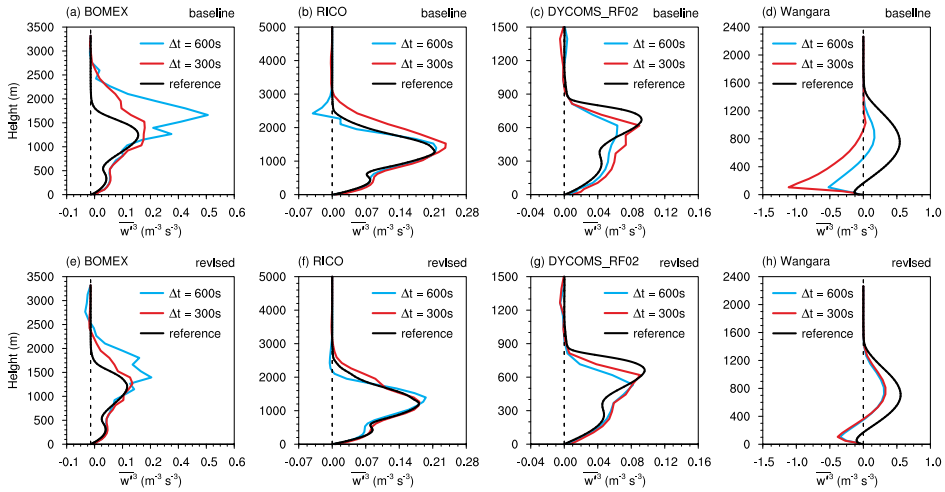

Figure 16. Mean profiles of the third order moments of vertical velocity ($\overline{w'^3}$, unit: $m^3\ s^{-3}$) from the simulations for BOMEX (first column) and RICO (second column) cumulus cloud cases, DYCOMS_RF02 stratocumulus cloud (third column) and Wangara dry turbulence (fourth column) cases. The mean quantities are derived by averaging the instantaneous model output during the first 6-hr period. The simulations were conducted with the baseline configuration in Table A2 for the first row (panels a–d), and the revised configuration in Table A2 for the second row (panels e–h). The solid black lines ("reference" in the legend) in panels (a-h) use $(\Delta z_0, \Delta t_0)/2^7$ with Δz_0 refers to as the reference model grid in Fig 1 and $\Delta t_0 = 4$ s. The red lines use $(\Delta z_0, 300\text{ s})$ that is closed to the vertical resolution and time step size for CLUBB in the EAM model. **The revised configuration improves the agreement of solutions between low-resolution $(\Delta z_0, 300\text{ s})$ and high-resolution $(\Delta z_0, \Delta t_0)/2^7$) simulations in panels e–h.**

and Wangara (Fig. B9 in appendix) cases. However, the improvements are relatively weak in RICO (Fig. B7 in appendix) and DYCOMS_RF02 (Fig. B8 in appendix).

Finally, the code changes in the revised configuration are also beneficial for the solution convergence in the simulations with the coupling of CLUBB with other parameterizations. Here, we show an example of space-time convergence from a simulation that couples CLUBB with a simplified radiation parameterization (see Eq.(13) of Larson et al. (2007)). The key radiative processes including cloud-top radiative cooling and cloud-based radiative heating in the radiation parameterization are important for the development of stratocumulus (e.g. DYCOMS_RF02 case) and boundary layer turbulence as they promote a sharp inversion, downward motions, and turbulent convective overturning (Guo et al., 2019). Compared to the baseline configuration (Fig. 17a–b), substantial improvements in the space-time convergence of $\overline{\theta_l}$ and $\overline{w'^3}$ during the 6-h period are achieved by the revised configuration (Fig. 17c–d), as well as other prognostic variables not shown here. Overall, we conclude that the better discretization in CLUBB can be also advantageous for the simulation with the radiation coupling, despite the fact that it does not always lead to first-order convergence (see $\overline{w'^3}$ at hour 2 and hour 3 of Fig. 17d). The lack of convergence in all variables and time periods suggest that pathologies do still remain in the revised configuration of CLUBB that will be addressed in future work.

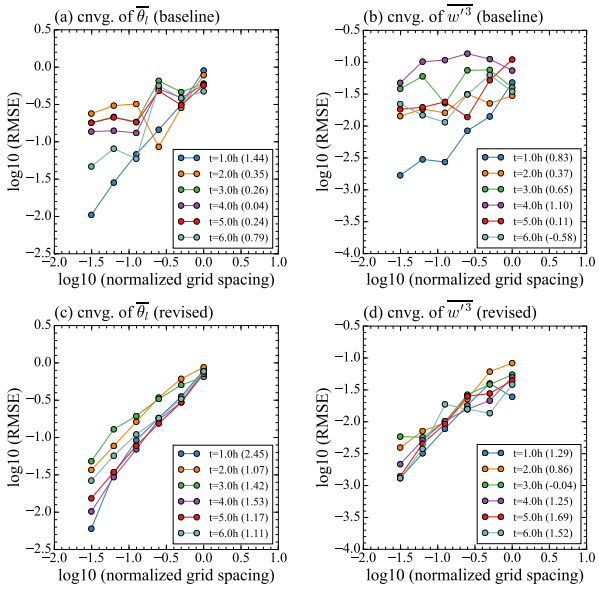

Figure 17. Space-time convergence with respect to the reference solution for (a–b) liquid potential temperature ($\overline{\theta_l}$) and (c–d) third order moments ($\overline{w'^3}$) from the simulations for DYCOMS_RF02 stratocumulus cloud case. All simulations were conducted with the revised configuration in Table A2, and CLUBB is coupled with a simplified radiation parameterization proposed by Larson et al. (2007) (see Eq.(13) in their paper). The reference solution is derived from the simulation that refines the reference model grid in Fig. 1a and time step (4 s) by a factor of 2^7. The convergence test was conducted as in Figure 2, and the RMSE and convergence rates shown in this figure are defined as in Figure 2. **Compared to the baseline configuration, the revised configuration also restores the expected first-order convergence of prognostic variables when CLUBB is coupled with a radiation parameterization**.

6 Conclusion and discussion

In this study, self-convergence testing with respect to time step and vertical grid spacing is employed to verify the discretization of the CLUBB parameterization of clouds and turbulence. The convergence testing has identified two general sources of discretization issues in CLUBB that may also exist in other parameterizations:

1. Unintended solution behavior can be introduced when a field is limited by a minimum function, a maximum function, or a Heaviside function. For instance, limiting a field using a max statement may lead to a discontinuity or slope discontinuity in that field (Section 4.1). If and when the limit is hit, then unphysical oscillations will be injected abruptly into the solution. The issue is exacerbated by CLUBB's use of centered finite difference schemes that are not well suited for sharp and discontinuous features. The presence of such pathologies will usually degrade self-convergence, and hence self-convergence testing provides a valuable diagnostic. Developers should be aware that introducing a limiter into a physics parameterization may alter solution behavior in a nonphysical way that is amplified when model resolution is changed.
2. Numerical diffusion of the kind shown in Eq. (18) can be decomposed into a pure diffusion term and an advection term. The advection term will either compress or extend profile features, depending on the profile of the advection velocity. Thus, the advection can actually sharpen features that perhaps the eddy diffusion term was intended to smooth. The sharpening can trigger spurious oscillations that degrade the solution fidelity and self convergence (see discussion in Section 4.2). These pathological features can be avoided by omitting the advection term and retaining only the pure diffusion term. This better fulfills the intended smoothing expected from numerical diffusion in CLUBB.

In addition, our analysis indicates that the initial and boundary conditions in atmospheric models ought to be formulated in terms of altitude rather than vertical grid spacing. Otherwise, the initial and boundary conditions can lead to unintended sensitivity of the model solution as the model resolution is refined (see results in Section 3). In addition, such an inappropriate formulation can prevent self-convergence even if the model equations in themselves are convergent. This can mislead us into thinking that a model implementation is defective when in fact it is not.

When the aforementioned problems are fixed in CLUBB, the unphysical oscillations are reduced (see Fig. 14) and the expected first-order convergence is achieved (see Figs. 15 and B5). Satisfyingly, the improvements in the solutions from the finer resolution simulations with small time-step sizes are also beneficial for the solutions at coarser resolution and large time step (see Fig. 16). Although the improvements at coarse resolution do not appear in all cases, our results indicate that understanding and improving the solution convergence can be a useful practice for model development of atmospheric parameterizations in climate models.

Appendix A Prognostic variables and *namelist* configurations in CLUBB-SCM

Table A1. Description of prognostic variables in CLUBB-SCM.

Variable	Description	Model level	Prognostic equations in Larson (2017)
$\overline{r_t}$	Total water content	thermodynamic	Eq. (4.1)
$\overline{\theta_l}$	Liquid water potential temperature	thermodynamic	Eq. (4.2)
$\overline{u}$	Zonal wind	thermodynamic	Eq. (4.3)
$\overline{v}$	Meridional wind	thermodynamic	Eq. (4.4)
$\overline{w'r_t'}$	Turbulent heat flux	momentum	Eq. (4.5)
$\overline{w'\theta_l'}$	Turbulent water flux	momentum	Eq. (4.6)
$\overline{u'w'}$	Turbulent momentum flux ($\overline{u}$)	momentum	Eq. (4.7)
$\overline{v'w'}$	Turbulent momentum flux ($\overline{v}$)	momentum	Eq. (4.7)
$\overline{r_t'^2}$	Variance of $\overline{r_t}$	momentum	Eq. (4.8)
$\overline{\theta_t'^2}$	Variance of $\overline{\theta_l}$	momentum	Eq. (4.9)
$\overline{r_t'\theta_l'}$	Covariance between $\overline{r_t}$ and $\overline{\theta_l}$	momentum	Eq. (4.10)
$\overline{u'^2}$	Variance of $\overline{u}$	momentum	Eq. (4.13)
$\overline{v'^2}$	Variance of $\overline{v}$	momentum	Eq. (4.14)
$\overline{w'^2}$	Variance of vertical velocity	momentum	Eq. (4.11)
$\overline{w'^3}$	Third-order moments of vertical velocity	thermodynamic	Eq. (4.12)

Table A2. List of the key *namelist* variables that were changed and/or added by this study to achieve the first order convergence in CLUBB-SCM simulations for the cases of BOMEX, RICO, DYCOMS_RF02 and Wangara. The setups in the default configuration are the same as the operational CLUBB-SCM that is available at `https://github.com/larson-group/clubb_release`. The baseline configuration is the same as the default configuration, except with the changes in the initial and boundary conditions (the flags in olive colors) that are discussed in Section 3. The code with all changes for the revised configuration can be found in `https://github.com/zhangshixuan1987/clubb_release/tree/best_convergence_fnl`. The flags in blue colors are related to the changes for the limiters and Heaviside function in turbulence moisture flux equation discussed in Section 4.1, while flags in red color related to the changes for the numerical diffusion terms discussed in Section 4.2. See the main text for the detailed descriptions of the related code changes and their impacts.

&configurable_clubb_flags_nl	Default configuration	Baseline configuration	Revised configuration
l_standard_term_ta	.True.	.True.	.True.
l_bc_at_constant_height	.False.	.True.	.True.
l_mono_cubic_sounding	.False.	.True.	.True.
l_new_dycoms2_sounding	.False.	.True.	.True.
l_smth_Heaviside_tau_wpxp	.False.	.False.	.True.
l_bvf_max_limiter	.True.	.True.	.False.
l_pure_diffusion	.False.	.False.	.True.

Appendix B Supplemental figures

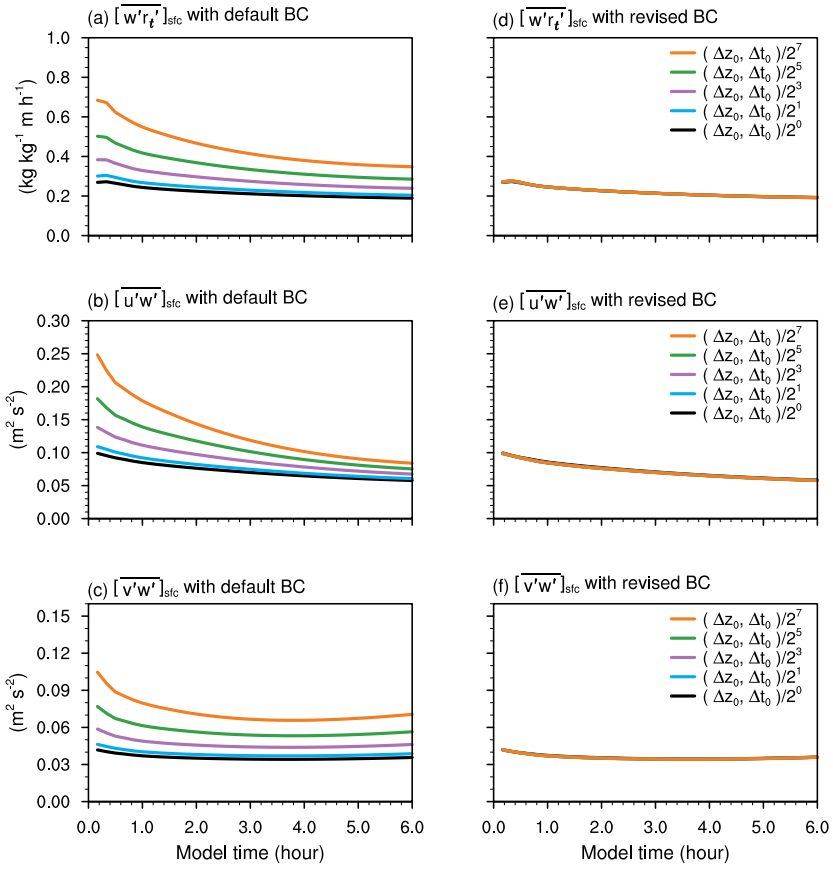

Figure B1. Time evolution of surface moisture ($[\overline{w'r_t'}]_{sfc}$, unit: kg kg^{-1} m h^{-1}, panels a and d), zonal momentum ($[\overline{u'w'}]_{sfc}$, unit: m^2 s^{-2}, panels b and e) and meridional momentum ($[\overline{v'w'}]_{sfc}$, unit: m^2 s^{-2}, panels c and f) fluxes during the 6-h period of simulations for RICO cumulus cloud case using various vertical resolutions. The simulations were conducted with the default configuration in Table A2, except with "l_bc_at_constant height = .false." for the first column (panels a–d) and "l_bc_at_constant height = .true." for the second column (panels e–h). The former represents the default setup of surface fluxes in which the bottom model levels changes with the resolution, while the latter represents the revised setup in which the surface fluxes are calculated at a constant model level located at 20 m. **With the default setup of boundary condition (BC), the surface fluxes vary with resolution (panels a–c).**

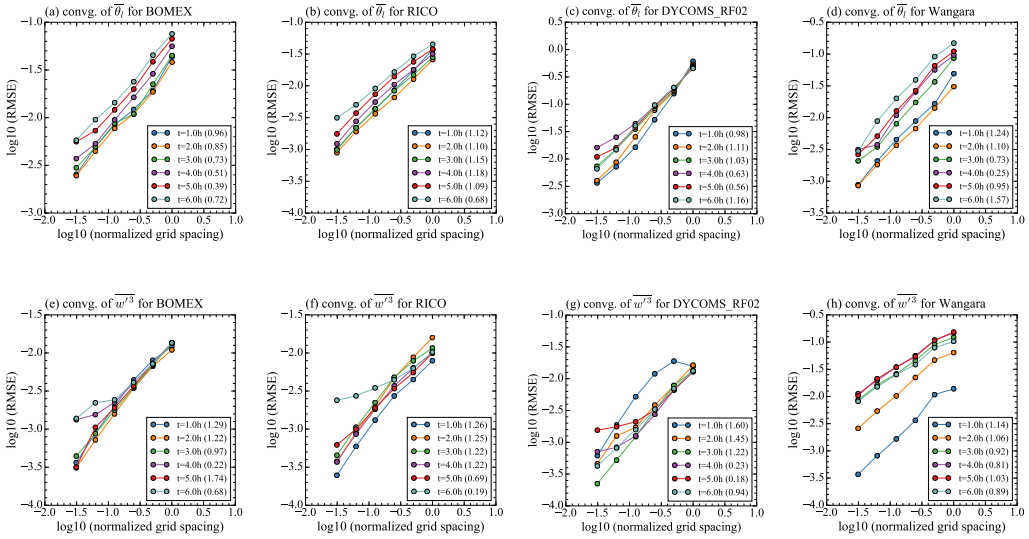

Figure B2. Space-time convergence with respect to the reference solution for liquid water potential temperature ($\overline{\theta_l}$, first row) and third-order moment of vertical velocity ($\overline{w'^3}$, second row) from the simulations for BOMEX (panels a and e), RICO (panels b and f), DYCOMS_RF02 (panels c and g), and Wangara (panels d and h). The simulations were conducted with the baseline configuration in Table A2, in which the revised initial and boundary conditions are activated in the CLUBB standalone model. The convergence test was conducted as in Figure 2, and the RMSE and convergence rates shown in this figure are defined as in Figure 2. **We note that the revised initial and boundary conditions lead to noticeable improvements of convergence in the RICO and dycoms2_rf02 cases, as compared with the operational results shown in Fig. 2**.

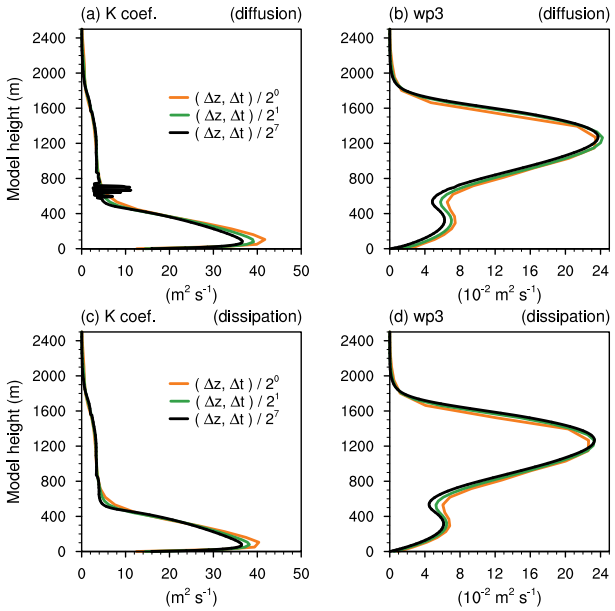

Figure B3. Profiles of the non-linear diffusion coefficient (K, unit: $m^2\ s^{-1}$, first column),and the third-order moment of vertical velocity ($\overline{w'^3}$, unit: $m^3\ s^{-3}$, second column) from the simulation for BOMEX cumulus cloud case. The instantaneous model output at hour 4 of the simulation is used to derive the plots. The simulations were conducted with the baseline configuration in Table A2, except with "l_pure_diffusion = .false." for the first row (panels (a–d)), while "l_pure_diffusion = .true." for the second row (panels (e–h)). The former represents the default setup with diffusion formulated as in Eq. (18) which contains both dissipation and advection components, while the latter represents the revised setup by changing diffusion to dissipation that is formulated as the first right-hand term in Eq. (19). **Changing the diffusion to dissipation leads to similar vertical variations of K_h and $\overline{w'^3}$, while the unphysical sawtooth-shaped oscillation of K_h at 400–800 m region is eliminated (panel (a) versus panels (c)).**

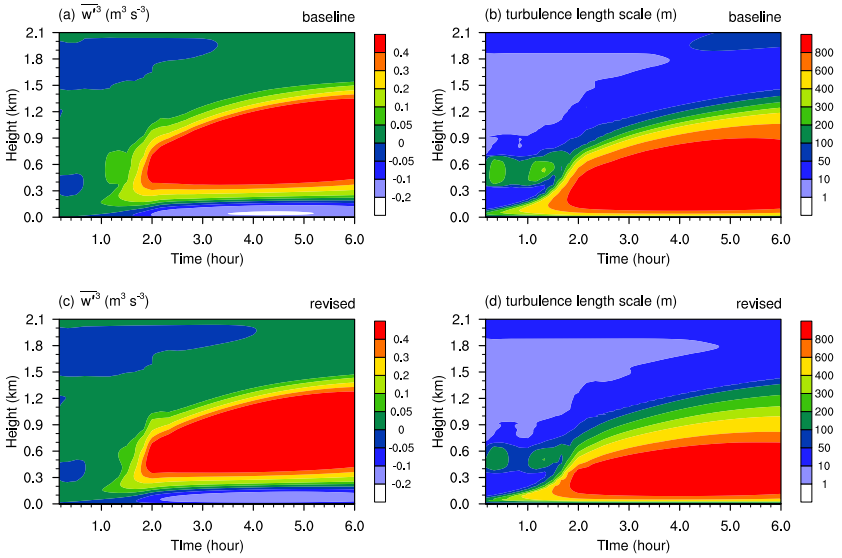

Figure B4. Hovmöller diagrams of the third order moments of vertical velocity ($\overline{w'^3}$, unit: m^3 s^{-3}, first column) and turbulence length scale (L_{scale}, unit: m, second column) from the simulation for Wangara dry turbulence case. The simulations were conducted with $(\Delta z_0, \Delta t_0)/2^7$ using the baseline configuration in Table A2 for the first row (panels (a–b)), and the revised configuration in Table A2 for the second row (panels (c–d)). Δz_0 is the reference model grid in Fig 1, and $\Delta t_0 = 4$ s. **The simulated $\overline{w'^3}$ and L_{scale} in the Wangara case show very similar features in the simulations with the baseline and revised configurations in Table A2**.

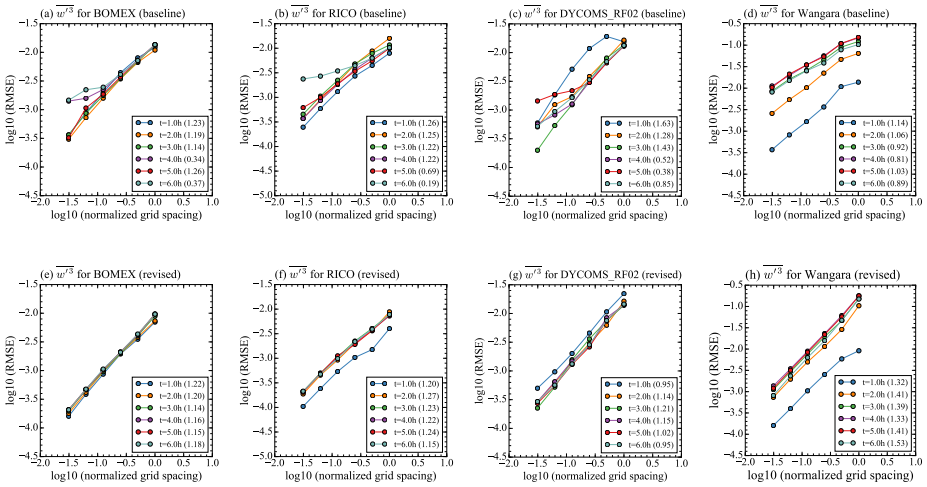

Figure B5. As in Figure 15 but showing the results for the liquid water potential temperature ($\overline{\theta_l}$) from the simulations with baseline (panels a–d) and revised (panels e–h) configurations in Table A2. **Compared to the baseline configuration (panels a–d), the revised configuration with the proposed code changes in CLUBB restores the expected first-order convergence in all four cases (panels e–h)**.

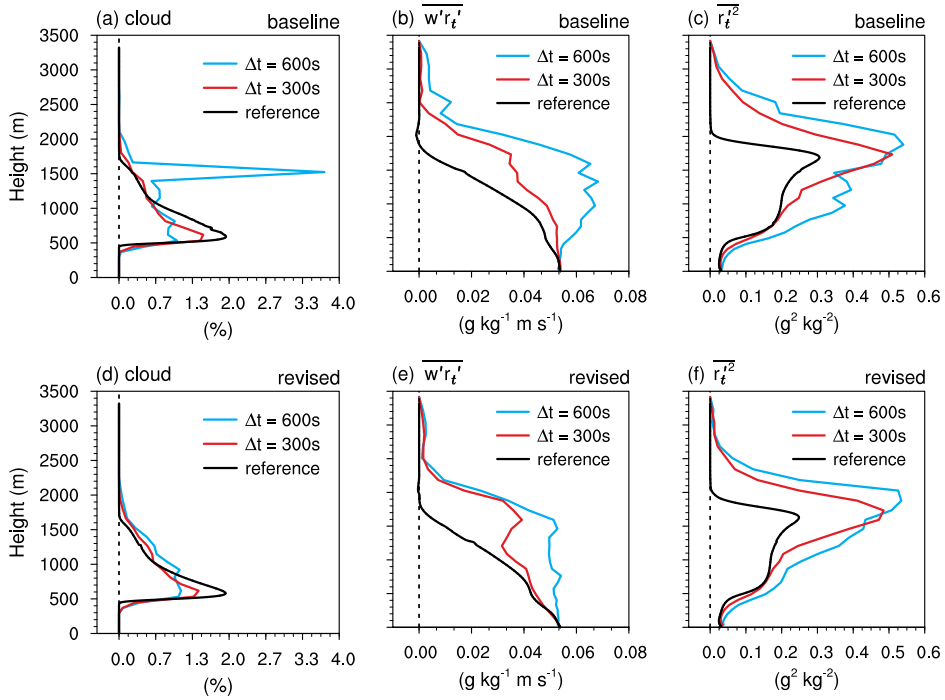

Figure B6. Mean profiles of cloud fraction (unit: %, first column), turbulence moisture fluxes ($\overline{w'r_t'}$, unit: $g\ kg^{-1}\ m\ s^{-1}$, second column) and variance of total water ($\overline{r_t'^2}$, unit: $g^2\ kg^{-2}$, third column) from the simulation for BOMEX cumulus cloud. The mean quantities are derived by averaging the instantaneous model output during 0–6 h period. The simulations were conducted with the baseline configuration in Table A2 for the first row (panels (a–d)), and the revised configuration in Table A2 for the second row (panels (e-h)). The solid black lines ("reference" in the legend) in panels (a-h) use $(\Delta z_0, \Delta t_0)/2^7$ with Δz_0 refers to the model grid in Fig 1, and $\Delta t_0 = 4$ s. The blue and red lines use $(\Delta z_0, 600\text{ s})$ and $(\Delta z_0, 300\text{ s})$, respectively. The latter is similar to the vertical resolution and model time step for CLUBB in the EAM model. **The revised configuration substantially reduces the discrepancies between simulations with lower temporal and spatial resolutions (red and blue lines) and simulations with high spatial and temporal resolutions (black lines) in panels (d–f).**

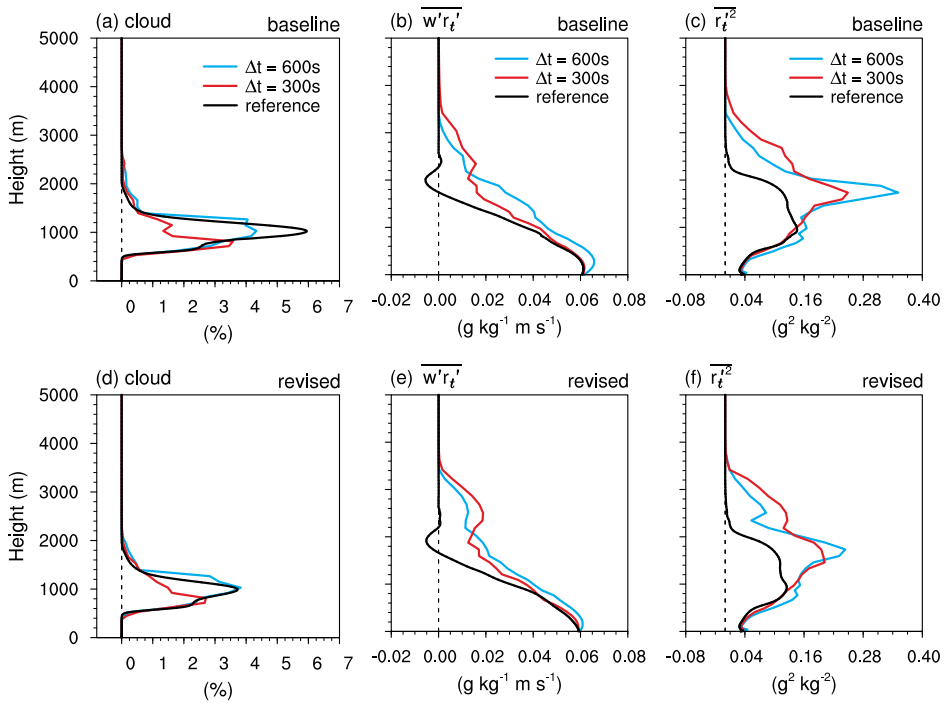

Figure B7. As in Figure B6 but showing the results for the RICO cumulus case. **The agreement between simulations with lower temporal and spatial resolutions (red and blue lines) and simulations with high spatial and temporal resolutions (black lines) are not significantly improved by the revised configuration for the physical quantities in panels (d–f).**

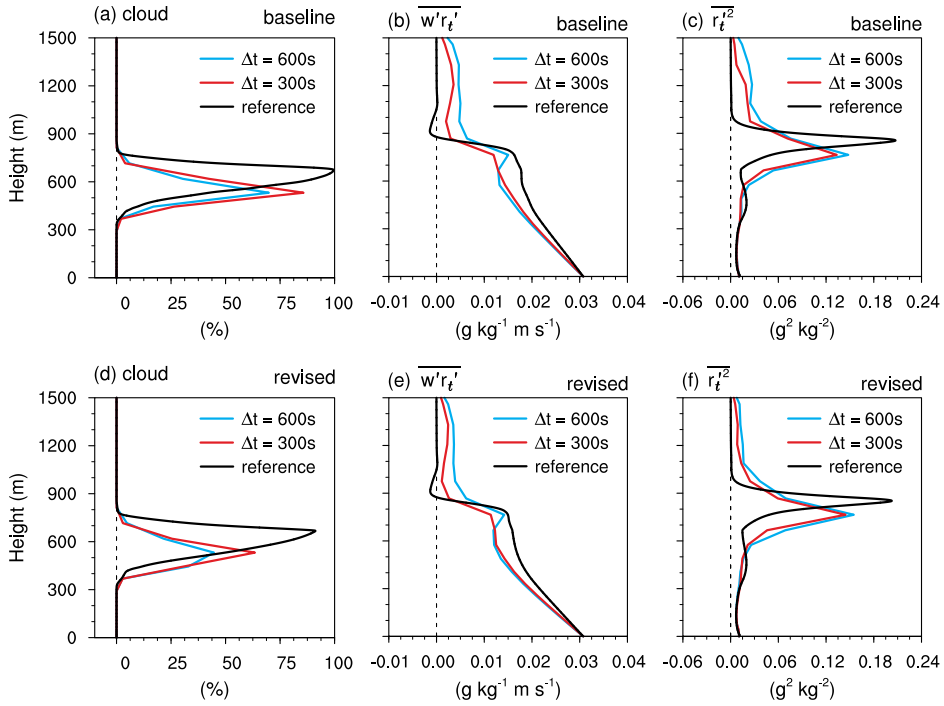

Figure B8. As in Figure B6 but showing the results for the DYCOMS_RF02 stratocumulus case. **The agreement between the simulation with Δt = 300 s (red lines) and the truth (black lines) are not significantly improved with the revised configuration, but the revised configuration with better solution convergence increase our confidence on these numerical results from CLUBB**.

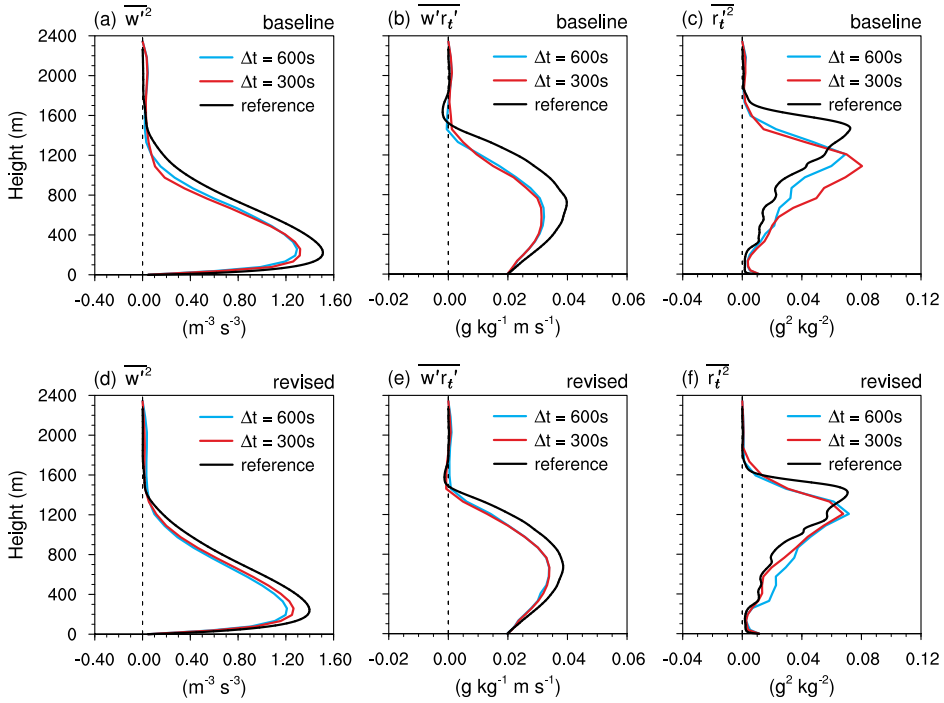

Figure B9. As in Figure B6 but showing the results for the Wangara dry turbulence case. **Compared to the baseline configuration, the revised configuration leads to improved agreement between the simulations with $\Delta t = 600$ s (red lines) and $\Delta t = 300$ s (blue lines) and the truth (black lines).**

Acknowledgments

The authors thank Panos Stinis for valuable discussions. This research has been supported by DOE BER and Office of Advanced Scientific Computing Research (ASCR), via the Scientific Discovery through Advanced Computing (SciDAC) program (grant no. 70276).

The CLUBB standalone model code was obtained from `https://github.com/larson-group/clubb_release`. The revised model code with all changes discussed in this study can be found on Zenodo at `https://doi.org/10.5281/zenodo.6385288` (CLUBB developers et al., 2022). The data for the analyses in this study can be found on Zenodo at `https://doi.org/10.5281/zenodo.6385559` (S. Zhang et al., 2022).

Computing resources for simulations shown in this paper were carried out using the DOE Biological and Environmental Research (BER) Earth System Modeling program's Compy computing cluster located at Pacific Northwest National Laboratory (PNNL) and using the Livermore Computing Center at Lawrence Livermore National Laboratory (LLNL). PNNL is operated by Battelle Memorial Institute for the U.S. Department of Energy under Contract DE-AC05-76RL01830. Work at LLNL was performed under the auspices of the U.S. Department of Energy by Lawrence Livermore National Laboratory under Contract DE-AC52-07NA27344. LLNL-JRNL-833507-DRAFT.

References

Clarke, R. H. (1971). *The wangara experiment : boundary layer data.* Australia: Div. Meteor. Phys. CSIRO.

CLUBB developers, Zhang, S., Vogl, C. J., & Larson, V. E. (2022). *Clubb single-column model source code for simulations in zhang et. al. (2022, james).* Zenodo. Retrieved from `https://doi.org/10.5281/zenodo.6385288` doi: 10.5281/zenodo.6385288

Golaz, J.-C., Larson, V. E., & Cotton, W. R. (2002). A pdf-based model for boundary layer clouds. part ii: Model results. *Journal of the Atmospheric Sciences*, *59*(24), 3552 - 3571. Retrieved from `https://journals.ametsoc.org/view/journals/atsc/59/24/1520-0469_2002_059_3552_apbmfb_2.0.co_2.xml` doi: 10.1175/1520-0469(2002)059⟨3552:APBMFB⟩2.0.CO;2

Guo, Z., Griffin, B. M., Domke, S., & Larson, V. E. (2021). A parameterization of turbulent dissipation and pressure damping time scales in stably stratified inversions, and its effects on low clouds in global simulations. *J. Adv. Model. Earth Syst.*, *13*, e2020MS002278. doi: 10.1029/2020MS002278

Guo, Z., Wang, M., Larson, V. E., & Zhou, T. (2019). A cloud top radiative cooling model coupled with clubb in the community atmosphere model: Description and simulation of low clouds. *Journal of Advances in Modeling Earth Systems*, *11*(4), 979-997. doi: https://doi.org/10.1029/2018MS001505

Holland, J. Z., & Rasmusson, E. M. (1973). Measurements of the atmospheric mass, energy, and momentum budgets over a 500-kilometer square of tropical ocean. *Monthly Weather Review*, *101*(1), 44 - 55. doi: 10.1175/1520-0493(1973)101⟨0044:MOTAME⟩2.3.CO;2

Holtslag, A. A. M., & Moeng, C.-H. (1991). Eddy diffusivity and countergradient transport in the convective atmospheric boundary layer. *Journal of Atmospheric Sciences*, *48*(14), 1690 - 1698. doi: 10.1175/1520-0469(1991)048⟨1690:EDACTI⟩2.0.CO;2

Knupp, P., & Salari, K. (2002). *Verification of computer codes in computational science and engineering.* Chapman and Hall/CRC.

Larson, V. E. (2017). Clubb-silhs: A parameterization of subgrid variability in the atmosphere. *arXiv preprint arXiv:1711.03675*.

Larson, V. E., Kotenberg, K. E., & Wood, N. B. (2007). An analytic longwave radiation formula for liquid layer clouds. *Monthly Weather Review*, *135*(2), 689 - 699. Retrieved from `https://journals.ametsoc.org/view/journals/mwre/135/2/mwr3315.1.xml` doi: 10.1175/MWR3315.1

Lin, C.-L., Lee, H., Lee, T., & Weber, L. J. (2005). A level set characteristic galerkin finite element method for free surface flows. *International Journal for Numerical Methods in Fluids*, *49*(5), 521-547. doi: https://doi.org/10.1002/fld.1006

Nakamura, N. (2001). A new look at eddy diffusivity as a mixing diagnostic. *Journal of the Atmospheric Sciences*, *58*(24), 3685 - 3701. doi: 10.1175/1520-0469(2001)058⟨3685:ANLAED⟩2.0.CO;2

Oberkampf, W. L., Trucano, T. G., & Hirsch, C. (2004). Verification, validation, and predictive capability in computational engineering and physics. *Applied Mechanics Reviews*, *57*, 345-384. doi: 10.1115/1.1767847

Rasch, P. J., Xie, S., Ma, P.-L., Lin, W., Wang, H., Tang, Q., ... Yang, Y. (2019). An overview of the atmospheric component of the energy exascale earth system model. *Journal of Advances in Modeling Earth Systems*, *11*(8), 2377-2411. doi: https://doi.org/10.1029/2019MS001629

Rauber, R. M., Stevens, B., Ochs, H. T., Knight, C., Albrecht, B. A., Blyth, A. M., ... Zuidema, P. (2007). Rain in shallow cumulus over the ocean: The rico campaign. *Bulletin of the American Meteorological Society*, *88*(12), 1912 - 1928. Retrieved from `https://journals.ametsoc.org/view/journals/bams/88/12/bams-88-12-1912.xml` doi: 10.1175/BAMS-88-12-1912

Rípodas, P., Gassmann, A., Förstner, J., Majewski, D., Giorgetta, M., Korn, P., ...

Heinze, T. (2009). Icosahedral shallow water model (icoswm): results of shallow water test cases and sensitivity to model parameters. *Geoscientific Model Development*, *2*(2), 231–251. Retrieved from https://gmd.copernicus.org/articles/2/231/2009/ doi: 10.5194/gmd-2-231-2009

Roache, P. J. (1998). *Verification and validation in computational science and engineering* (Vol. 895). Hermosa Albuquerque, NM.

Siebesma, A. P., Bretherton, C. S., Brown, A., Chlond, A., Cuxart, J., Duynkerke, P. G., ... Stevens, D. E. (2003). A large eddy simulation intercomparison study of shallow cumulus convection. *Journal of the Atmospheric Sciences*, *60*(10), 1201 - 1219. Retrieved from https://journals.ametsoc.org/view/journals/atsc/60/10/1520-0469_2003_60_1201_alesis_2.0.co_2.xml doi: 10.1175/1520-0469(2003)60⟨1201:ALESIS⟩2.0.CO;2

Siebesma, A. P., Soares, P. M. M., & Teixeira, J. (2007). A combined eddy-diffusivity mass-flux approach for the convective boundary layer. *Journal of the Atmospheric Sciences*, *64*(4), 1230 - 1248. doi: 10.1175/JAS3888.1

Stevens, B. (2000). Quasi-steady analysis of a pbl model with an eddy-diffusivity profile and nonlocal fluxes. *Monthly Weather Review*(3), 824 - 836. doi: 10.1175/1520-0493(2000)128⟨0824:QSAOAP⟩2.0.CO;2

Stevens, B., Ackerman, A. S., Albrecht, B. A., Brown, A. R., Chlond, A., Cuxart, J., ... Stevens, D. E. (2001). Simulations of trade wind cumuli under a strong inversion. *Journal of the Atmospheric Sciences*, *58*(14), 1870 - 1891. doi: 10.1175/1520-0469(2001)058⟨1870:SOTWCU⟩2.0.CO;2

Stevens, B., Lenschow, D. H., Vali, G., Gerber, H., Bandy, A., Blomquist, B., ... van Zanten, M. C. (2003). Dynamics and chemistry of marine stratocumulus—dycoms-ii. *Bulletin of the American Meteorological Society*, *84*(5), 579 - 594. Retrieved from https://journals.ametsoc.org/view/journals/bams/84/5/bams-84-5-579.xml doi: 10.1175/BAMS-84-5-579

Stinis, P., Lei, H., Li, J., & Wan, H. (2020). Improving solution accuracy and convergence for stochastic physics parameterizations with colored noise. *Monthly Weather Review*, *148*(6), 2251 - 2263. doi: 10.1175/MWR-D-19-0178.1

Stuhne, G., & Peltier, W. (1999). New icosahedral grid-point discretizations of the shallow water equations on the sphere. *Journal of Computational Physics*, *148*(1), 23-58. doi: https://doi.org/10.1006/jcph.1998.6119

Suselj, K., Kurowski, M. J., & Teixeira, J. (2019). A unified eddy-diffusivity/mass-flux approach for modeling atmospheric convection. *Journal of the Atmospheric Sciences*, *76*(8), 2505 - 2537. doi: 10.1175/JAS-D-18-0239.1

Sussman, M. B., Fatemi, E., Osher, S. J., & Smereka, P. (1994). A level set approach for computing solutions to incompressible two- phase flow ii..

Taylor, M., Tribbia, J., & Iskandarani, M. (1997). The spectral element method for the shallow water equations on the sphere. *Journal of Computational Physics*, *130*(1), 92-108. doi: https://doi.org/10.1006/jcph.1996.5554

vanZanten, M. C., Stevens, B., Nuijens, L., Siebesma, A. P., Ackerman, A. S., Burnet, F., ... Wyszogrodzki, A. (2011). Controls on precipitation and cloudiness in simulations of trade-wind cumulus as observed during rico. *Journal of Advances in Modeling Earth Systems*, *3*(2). doi: https://doi.org/10.1029/2011MS000056

Vogl, C. J., Wan, H., Zhang, S., Woodward, C. S., & Stinis, P. (2020). Improving time step convergence in an atmosphere model with simplified physics: Using mathematical rigor to avoid nonphysical behavior in a parameterization. *Journal of Advances in Modeling Earth Systems*, *12*(10), e2019MS001974. Retrieved from https://agupubs.onlinelibrary.wiley.com/doi/abs/10.1029/2019MS001974 doi: https://doi.org/10.1029/2019MS001974

Wan, H., Woodward, C. S., Zhang, S., Vogl, C. J., Stinis, P., Gardner, D. J., ... Singh, B. (2020). Improving time step convergence in an atmosphere model with simplified physics: The impacts of closure assumption and pro-

cess coupling. *Journal of Advances in Modeling Earth Systems*, *12*(10), e2019MS001982. Retrieved from `https://agupubs.onlinelibrary.wiley.com/doi/abs/10.1029/2019MS001982` doi: https://doi.org/10.1029/2019MS001982

Wan, H., Zhang, S., Rasch, P. J., Larson, V. E., Zeng, X., & Yan, H. (2021). Quantifying and attributing time step sensitivities in present-day climate simulations conducted with eamv1. *Geoscientific Model Development*, *14*(4), 1921–1948. doi: 10.5194/gmd-14-1921-2021

Wyant, M. C., Bretherton, C. S., Chlond, A., Griffin, B. M., Kitagawa, H., Lappen, C.-L., ... Ackerman, A. S. (2007). A single-column model intercomparison of a heavily drizzling stratocumulus-topped boundary layer. *Journal of Geophysical Research*, *112*.

Xie, S., Lin, W., Rasch, P. J., Ma, P.-L., Neale, R., Larson, V. E., ... Zhang, Y. (2018). Understanding cloud and convective characteristics in version 1 of the e3sm atmosphere model. *Journal of Advances in Modeling Earth Systems*, *10*(10), 2618-2644. doi: https://doi.org/10.1029/2018MS001350

Zhang, K., O'Donnell, D., Kazil, J., Stier, P., Kinne, S., Lohmann, U., ... Feichter, J. (2012). The global aerosol-climate model echam-ham, version 2: sensitivity to improvements in process representations. *Atmospheric Chemistry and Physics*, *12*(19), 8911–8949. doi: 10.5194/acp-12-8911-2012

Zhang, S., Vogl, C. J., & Larson, V. E. (2022). *CLUBB single-column model output and scripts for analyses in Zhang et. al. (2022, JAMES).* Zenodo. Retrieved from `https://doi.org/10.5281/zenodo.6385560` doi: 10.5281/zenodo.6385560